

## Balancing prediction accuracy and generalization ability: A hybrid framework for modelling the annual dynamics of satellite-derived land surface temperatures



Zihan Liu<sup>a</sup>, Wenfeng Zhan<sup>a,b,\*</sup>, Jiameng Lai<sup>a</sup>, Falu Hong<sup>a</sup>, Jinling Quan<sup>c</sup>, Benjamin Bechtel<sup>d</sup>, Fan Huang<sup>a</sup>, Zhaoxu Zou<sup>a</sup>

<sup>a</sup> Jiangsu Provincial Key Laboratory of Geographic Information Science and Technology, International Institute for Earth System Science, Nanjing University, Nanjing, Jiangsu 210023, China

<sup>b</sup> Jiangsu Center for Collaborative Innovation in Geographical Information Resource Development and Application, Nanjing 210023, China

<sup>c</sup> State Key Laboratory of Resources and Environmental Information System, Institute of Geographic Sciences and Natural Resources Research, Chinese Academy of Sciences, Beijing 100101, China

<sup>d</sup> Center for Earth System Research and Sustainability, Universität Hamburg, 20146 Hamburg, Germany

### ARTICLE INFO

#### Keywords:

Land surface temperature  
Annual temperature cycle  
LST dynamics  
Prediction accuracy  
Generalization ability

### ABSTRACT

Annual temperature cycle (ATC) models enable the multi-timescale analysis of land surface temperature (LST) dynamics and are therefore valuable for various applications. However, the currently available ATC models focus either on prediction accuracy or on generalization ability and a flexible ATC modelling framework for different numbers of thermal observations is lacking. Here, we propose a hybrid ATC model (ATCH) that considers both prediction accuracy and generalization ability; our approach combines multiple harmonics with a linear function of LST-related factors, including surface air temperature (SAT), NDVI, albedo, soil moisture, and relative humidity. Based on the proposed ATCH, various parameter-reduction approaches (PRAs) are designed to provide model derivatives which can be adapted to different scenarios. Using Terra/MODIS daily LST products as evaluation data, the ATCH is compared with the original sinusoidal ATC model (termed the ATCO) and its variants, and with two frequently-used gap-filling methods (Regression Kriging Interpolation (RKI) and the Remotely Sensed DAily land Surface Temperature reconstruction (RSDAST)), under clear-sky conditions. In addition, under overcast conditions, the LSTs generated by ATCH are directly compared with *in-situ* LST measurements. The comparisons demonstrate that the ATCH increases the prediction accuracy and the overall RMSE is reduced by 1.8 and 0.7 K when compared with the ATCO during daytime and nighttime, respectively. Moreover, the ATCH shows better generalization ability than the RKI and behaves better than the RSDAST when the LST gap size is spatially large and/or temporally long. By employing LST-related controls (e.g., the SAT and relative humidity) under overcast conditions, the ATCH can better predict the LSTs under clouds than approaches that only adopt clear-sky information as model inputs. Further attribution analysis implies that incorporating a sinusoidal function (ASF), the SAT, NDVI, and other LST-related factors, provides respective contributions of around 16%, 40%, 15%, and 30% to the improved accuracy. Our analysis is potentially useful for designing PRAs for various practical needs, by reducing the smallest contribution factor each time. We conclude that the ATCH is valuable for further improving the quality of LST products and can potentially enhance the time series analysis of land surfaces and other applications.

### 1. Introduction

Land surface temperatures (LSTs) derived from satellite thermal remote sensing are vital for investigating global and regional climate change, carbon-hydrological cycles, and surface-atmosphere interactions (Jin et al., 2005; Weng, 2009; Kleidon and Renner, 2013; Kalma

et al., 2008). However, more than one-half of the satellite-derived LST data are missing due to the global prevalence of clouds (Sun et al., 2017), which has greatly limited the applications of LSTs. Previous research has attempted to produce spatio-temporally seamless LSTs, which can be grouped into two main categories: data- and model-driven methods (Crosson et al., 2012; Xu and Shen, 2013). In general, data-

\* Corresponding author at: Nanjing University at Xianlin Campus, No. 163 Xianlin Avenue, Qixia District, Nanjing, Jiangsu 210023, China.  
E-mail address: [zhanwenfeng@nju.edu.cn](mailto:zhanwenfeng@nju.edu.cn) (W. Zhan).

driven methods concentrate more on the use of the auxiliary data, whereas model-driven methods rely more on the incorporation of physical models that describe the spatio-temporal variations of LSTs. There is no clear boundary between these two categories of methods, despite the different strategies used: Some of the data-driven methods may incorporate simple physical models of LST variations (Ke et al., 2013), whereas model-driven methods occasionally require various auxiliary data (Zou et al., 2018).

Data-driven methods may use either auxiliary data from the same or different satellite sensors (Crosson et al., 2012; Hengl et al., 2012). They commonly call for the investigation of the statistical relationships between LSTs and auxiliary data (e.g., vegetation index, precipitation, terrain, and soil moisture) (Fan et al., 2014). In other words, they usually do not require a deep understanding of the LST dynamics and their performances; thus, they are critically dependent on the quality and quantity of the auxiliary data used. Model-driven methods, by contrast, rely more on the use of physical (or sometimes statistical) models that describe the temporal/spatial variations of LSTs (Bechtel, 2011; Fu and Weng, 2018; Ke et al., 2013; Sun et al., 2017; Pede and Mountrakis, 2018). Typical spatial models include inverse distance weighting (Liu et al., 2017), gradient plus inverse distance squared (Zhou et al., 2012), and Kriging and its variants (Hengl et al., 2012; Lyon et al., 2010). Studies have shown that these spatial models are usually good at filling discontinuous LSTs with spatially small and temporally short gaps (Liu et al., 2017; Pede and Mountrakis, 2018). By comparison, temporal models are regularly formulated at different timescales; they include the inter-annual temperature dynamics (ATD) model (Fu and Weng, 2016), intra-annual temperature cycle (ATC) model (Bechtel, 2011; Xu and Shen, 2013), and the diurnal temperature cycle (DTC) model (Duan et al., 2012). When compared with the spatial models, the temporal models are structurally better at filling discontinuous LSTs with spatially large and temporally long gaps and therefore they play a unique role in the gap-filling of LSTs (Liu et al., 2017).

As one among various temporal models, ATC models enable a continuous description of the LST cycle on an annual scale (Bechtel and Sismanidis, 2017; Fu and Weng, 2018). ATC models have been shown to be valuable in various applications such as the generation of daily LSTs (Fu and Weng, 2016), downscaling of LSTs (Zhan et al., 2016; Sismanidis et al., 2017), characterization of local climate zones (Bechtel, 2011), and monitoring of surface urban heat islands (Huang et al., 2016; Quan et al., 2016). The currently available ATC models can be divided into three groups. The first group uses a series of sinusoidal (harmonic) functions to simulate annual LST dynamics, such as the Harmonic ANalysis of Time Series (HANTS) (Xu and Shen, 2013). The HANTS can characterize LST dynamics and reconstruct LST data gaps with a generally high accuracy, although with a relatively complex form. The second group uses very few (only one or two) sinusoidal functions to characterize annual LST dynamics. For example, Bechtel (2011) proposed the use of a single sine function to model annual LST variations (henceforth termed the ATCO) and later suggested the use of two sine functions (henceforth termed the ATCT) for improved modelling (Bechtel and Sismanidis, 2017). These concise ATC models have a distinct physical basis and therefore they have an excellent generalization ability<sup>1</sup>, although their performances may be slightly lower. The abovementioned two groups of ATC models are temporally smooth, and they do not include terms that extract short-term LST fluctuations responding to weather and surface changes. To capture such short-term LST fluctuations, the third group of ATC models incorporate either statistical processes such as Gaussian process regression (Fu and Weng, 2016), or additional data such as *in-situ* surface air temperature and

vegetation index (Zou et al., 2018). Generally, concise models such as the ATCO typically have better generalization abilities due to the limited number of parameters, but their accuracy is relatively low. Models with relatively more sophisticated forms (e.g., the HANTS) have a higher accuracy, but their generalization abilities are relatively low due to the large number of parameters. In other words, although great progress has been made, the existing ATC models were developed to focus either on prediction accuracy or model efficiency. Consequently, a flexible ATC framework that simultaneously considers the prediction and generalization ability and that provides options for users under various practical needs is lacking.

In response to this challenge, this study aims to propose a flexible ATC framework, based on which we propose a hybrid ATC model with a balance between prediction accuracy and generalization ability. Specifically, we combine multiple harmonics with a linear function of LST-related factors to obtain a flexible ATC framework, specify the number of harmonic function and LST-related factors to balance model prediction accuracy and generalization ability, design various parameter-reduction approaches (PRAs) to provide model derivatives which can adapt to different scenarios, and evaluate the hybrid ATC model under clear and all-weather conditions. We consider that this hybrid model provides a better description of annual LST dynamics when temporally discontinuous LSTs are used as inputs, and it is therefore potentially helpful for improving LST products as well as for the associated applications.

## 2. Study area and data

### 2.1. Study area

Mainland China (67.9°E–136.5°E, 15.3°N–54.6°N) was selected as the study area (Fig. 1). China has a vast territory, wherein complex geological environments and climatic conditions have resulted in diverse land cover conditions. This diversity makes mainland China an ideal place to test model performances at a regional/continental scale. Note that in Fig. 1 we have masked the water bodies, which are not land surfaces.

### 2.2. Data

#### 2.2.1. Satellite data

The satellite data used in 2012 include the Moderate Resolution Imaging Spectroradiometer (MODIS) daily LST product MOD11A1 (onboard Terra satellite), 16-day normalized difference vegetation index (NDVI) product MOD13A2 (onboard Terra satellite), MODIS 16-day global albedo product MCD43A3, and MODIS yearly land cover product MCD12Q1. These satellite data can be acquired from the NASA Earth Science Data (<https://ladsweb.modaps.eosdis.nasa.gov/>). Both daytime (~10:30 am) and nighttime (~22:30 pm) LSTs from MOD11A1 were used; 19 MODIS tiles covering mainland China were used, and a sub-image with 4042 × 4841 pixels was then extracted to match the extent of mainland China. The resolutions of the MCD43A3 (0.5 km) and MCD12Q1 (0.5 km) were both resampled to 1 km to match that of the LST product. Detailed information on the satellite data are presented in Table 1.

#### 2.2.2. Meteorological data and surface measurements

Daily maximum and minimum surface air temperatures (SATs) from 2479 meteorological stations (<http://data.cma.cn/site/index.html>, see Fig. 1 for their locations) were used (Table 2). The SATs were resampled into raster images with a resolution of 1 km, using the IDW method, to match the LST data (Zou et al., 2018). At the pixel scale, we calculated the daily mean SATs with the daily maximum and minimum SAT images interpolated based on the *in-situ* measurements. Note that the daily mean SATs at those pixels wherein stations are located were designated directly using the corresponding available *in-situ* SATs. In

<sup>1</sup> Here, the model generalization ability is defined as the adaptation capability of a developed method for use with new input data or patterns (Schmidt and Bandar, 1998).

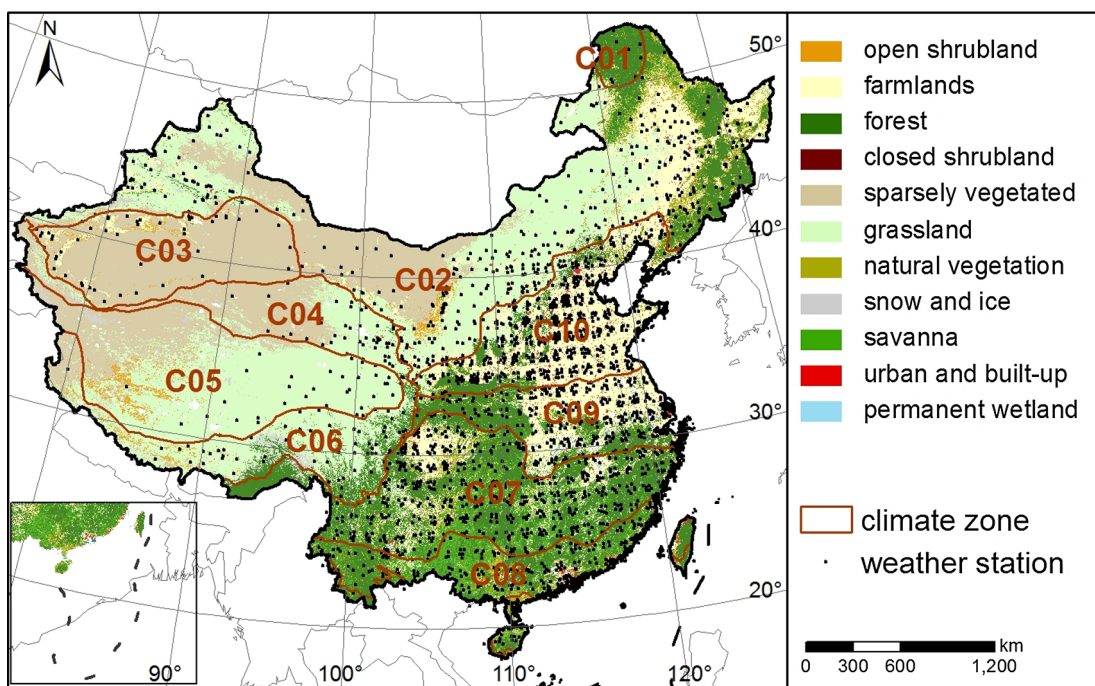


**Fig. 1.** Geolocation of the meteorological sites, land cover types and climate zones across mainland China. Ten climate zones (C01 to C10) were classified according to topographic and climatic characteristics (Zheng et al., 2010).

**Table 1**  
Details of the Satellite data used in this study.

Variable	Product	Number of tiles	Temporal/spatial resolution
LST	MOD11A1	19 × 366 × 2	Daily/1 km
NDVI	MOD13A2	19 × 23	16-day/1 km
Albedo	MCD43A3	19 × 23	16-day/0.5 km
Land cover	MCD12Q1	19 × 1	yearly/0.5 km

Note that there are '19 tiles over Mainland China × 366 day × 2 transits/day' of LST images in total.

**Table 2**  
Detailed information on the meteorological data and surface measurements used in this study.

Abbreviation	Product	Source	Temporal/spatial resolution
SAT	—	Meteorological stations	Daily/—
RH	Noah-LSM	GLDAS	3-h/0.25°
SM	Noah-LSM	GLDAS	3-h/0.25°
GST	—	SURFRAD stations	1-min/—

Henceforth, SAT, RH, SM and GST respectively represent surface air temperature, relative humidity, soil moisture and ground surface temperature.

**Table 3**  
Details of the seven sites chosen from the SURFRAD network.

Station	Lat./Long. (°)	Corresponding MODIS tile	Altitude (m)	Land cover type
Bondville (BON)	40.05/-88.37	h11v04	213	Cropland
Boulder (BCO)	40.13/-105.24	h09v04	1689	Grassland
Fort Peck (FPK)	48.31/-105.10	h11v04	634	Grassland
Goodwin Creek (GWN)	34.25/-89.87	h10v05	98	Grassland
Penn State (PST)	40.72/-77.93	h12v04	376	Cropland
Sioux Falls (SXF)	40.73/-96.62	h11v04	473	Grassland
Desert Rock (DRA)	36.63/-116.02	h08v05	1007	Desert

addition, the 0.25° relative humidity (RH) and soil moisture (SM) per 3-h, simulated with the common Global Land Data Assimilation System (GLDAS) in 2012 was included (see Table 2 for detailed information). Both datasets were obtained from the Goddard Earth Sciences Data and Information Services Center (GES DISC) (<https://disc.gsfc.nasa.gov/datasets/>). The RH and SM data were also resampled to 1 km. Note that only the RH and SM data from around the time of overpass of the Terra satellite were used.

Surface Radiation Budget Network (SURFRAD) ground measurements were also used (<https://www.esrl.noaa.gov/gmd/grad/surfrad/overview.html>). Due to the high quality of the surface measurements, the SURFRAD has been widely used for validating satellite-derived LSTs (Li et al., 2014; Zeng et al., 2018). The SURFRAD provides surface radiation and meteorological observations every 1 min in 2012. We followed the procedures of Zeng et al. (2018) to convert surface radiation to LST. Finally, the *in-situ* LST data from the seven sites of the SURFRAD were used to evaluate model performances under all-weather conditions. The surface types at the seven sites are mostly cropland, grassland and desert (Table 3).

### 3. Methodology

This section provides a complete technical description of the ATC modelling framework that is able to balance prediction accuracy and generalization ability. A full list of mathematical symbols and their

**Table 4**

List of abbreviations used in Eqs. (1)–(6).

Abbreviations	Description
$T_s$	The daily mean LST within an annual cycle
$T_{air}$	The daily mean SAT within an annual cycle
$T_0$	The annual mean of the annual LST cycle
$T_{0\_air}$	The annual mean of the annual SAT cycle
$A$	The amplitude of the annual LST cycle
$A_{air}$	The amplitude of the annual SAT cycle
$\theta$	The phase shift of the annual LST cycle
$\theta_{air}$	The phase shift of the annual SAT cycle
$\Delta T_{air}$	The day-to-day difference between the daily mean observed and predicted SAT by Eq. (4)
$t$	The day relative to the spring equinox
$d$	The number of days in an annual cycle, e.g., $d = 366$ for 2012
$\omega$	The constant calculated as $2\pi d^{-1}$
$a_1, b_1$	The coefficients for the sine and cosine function, respectively, and they represent the primary component of the annual LST dynamics
$a_n, b_n (n > 1)$	The coefficients for the sine and cosine function, respectively, and they represent the subordinate component of the annual LST dynamics
$\varphi$	The function of $T_s$ (i.e., daily mean LST) using $t$ (i.e., the day relative to the spring equinox) as the variable
$\varphi_1$	The revised function of $T_s$ using $t$ as the variable
$\psi$	The function of $\Delta T_{air}$ using $t$ as the variable
$\gamma_m$	The incorporated meteorological and surface factors in the proposed ATC modeling framework
$k_m$	The associated multipliers of the incorporated meteorological and surface factors
$M$	The number of incorporated meteorological and surface factors
$N$	The number of the used harmonics
$\gamma (\gamma_1, \gamma_2, \gamma_3, \gamma_4)$	The vector composed of the incorporated controls in the ATC modelling framework, including the daily NDVI, soil moisture, albedo, and relative humidity
$\mathbf{k} (k_1, k_2, k_3, k_4)$	The vector composed of the associated multipliers of the incorporated controls in the ATC modelling framework

meanings is provided in Table 4 in advance to help readers better understand the associated equations given as below.

### 3.1. Improving the accuracy of ATC modeling by disregarding generalization ability

From the perspective of remote sensing, a single sinusoidal function was proposed to model annual LST dynamics (Bechtel, 2011):

$$T_s(t) = \varphi(T_0, A, \theta, t) = T_0 + A \cdot \sin(\omega t + \theta) \quad (1)$$

Here,  $T_s(t)$  is the daily LSTs within an annual cycle;  $t$  is the day relative to the spring equinox;  $\varphi$  denotes the function between  $T_s$  and  $t$ ;  $T_0$ ,  $A$ , and  $\theta$  are respectively the annual mean, amplitude, and phase shift of the annual LST cycle; and  $\omega$  is a constant calculated by  $2\pi d^{-1}$ , where  $d$  represents the number of days in an annual cycle (e.g.,  $d = 366$  for 2012).

The ATC model given by Eq. (1) only considers the primary component (e.g., the incoming solar radiation) of the annual LST dynamics; i.e., it is unable to characterize fully the subordinate components of the LST variations within an annual cycle (Bechtel, 2011; Quan et al., 2016). To model both the primary and subordinate components of the LST dynamics, an increased number of harmonic are needed (Bechtel and Sismanidis, 2017; Xu and Shen, 2013). Elaborate explanations of the assumption in terms of the number of harmonic are provided in Appendix A. With an adequate number of harmonics incorporated, the annual LST dynamics can consequently be expressed by the following formula:

$$\begin{aligned} T_s(t) &= \varphi_1(T_0, a_1, \dots, a_n, b_1, \dots, b_n, \omega, t) \\ &= T_0 + \sum_{n=1}^N (a_n \sin n\omega t + b_n \cos n\omega t) \end{aligned} \quad (2)$$

Here,  $\varphi_1$  denotes the revised function between  $T_s$  and  $t$ ;  $N$  represents the number of harmonics used;  $a_1$  and  $b_1$  are the coefficients for the primary component of the annual LST dynamics; and  $a_n$  and  $b_n$  ( $n > 1$ ) are the coefficients of the subordinate components.

The ATC model given by Eq. (2), in theory, can fully characterize all the components of variation (i.e., from the yearly to daily timescale) of

the LST dynamics within an annual cycle when  $N$  approaches the number of days in a year (Brooks et al., 2012). However, the modeling of high-frequency LST variations (e.g., at the weekly/daily timescale) would involve a very large number of harmonics, which would therefore probably render the associated ATC model unstable. To formulate an ATC model that is sufficiently stable as well as capable of representing short-term LST fluctuations, the incorporation of ancillary data related to the LST variations is one option for improving the representation (Fu and Weng, 2018). Several studies have shown that information on the surface status (e.g., the NDVI) and on meteorological conditions (e.g., the *in-situ* SATs) are both valuable to help estimate the LST fluctuations due to the surface alterations and weather fluctuations, respectively (Zou et al., 2018). The detailed explanations on this model formation are also provided in Appendix A. With such ancillary data incorporated, the ATC model given by Eq. (2) can be reformulated as follows:

$$\begin{aligned} T_s(t) &= \varphi_1(T_0, a_1, \dots, a_n, b_1, \dots, b_n, \omega, t) + \psi(k, t) \\ &= T_0 + \sum_{n=1}^N (a_n \sin n\omega t + b_n \cos n\omega t) + \gamma(t) \cdot \mathbf{k} \cdot \Delta T_{air}(t) \end{aligned} \quad (3)$$

Here,  $\gamma(t)$  denotes the NDVI at time  $t$ ;  $\mathbf{k}$  is a multiplier that helps modulate the  $\Delta T_{air}(t)$ , which represents the difference between the daily mean SAT and fitted LSTs predicted using Eq. (1);  $\psi$  denotes the function between  $\gamma \Delta T_{air}$  and  $t$ .  $\Delta T_{air}(t)$  is calculated as Eq. (4). The  $\Delta T_{air}$  can be used to help characterize the LST variations because the differences between observed and modeled SATs are similar to those in the LSTs (Good, 2016; Good et al., 2017) (refer to Appendix A).

$$\Delta T_{air}(t) = T_{air}(t) - \varphi(T_{0\_air}, A_{air}, \theta_{air}, t) \quad (4)$$

where  $T_{air}(t)$  is the daily mean SATs, which is estimated as the mean between the daily maximum and minimum *in-situ* SATs;  $\varphi$  is the single sinusoidal function given by Eq. (1), with parameters  $T_{0\_air}$ ,  $A_{air}$ , and  $\theta_{air}$ , respectively representing the annual mean, amplitude, and phase shift of the annual SAT cycle.

Nevertheless, the use of the NDVI and a multiplier is insufficient to capture fully the daily LST-SAT differences (i.e.,  $\Delta T_{air}$ ), because various additional meteorological and surface conditions are as well as able to influence  $\Delta T_{air}$  (Lin et al., 2016), such as the soil moisture and relative

humidity (Kloog et al., 2014; Good, 2016) (refer to Appendix A). By incorporating more of such controls, herein we define a flexible ATC modeling framework (ATCF), which is expressed as:

$$\begin{aligned} T_s(t) &= \varphi_1(a_0, a_n, b_n, \omega, t) + \psi_1(k_m, t) \\ &= T_0 + \sum_{n=1}^N (a_n \sin n\omega t + b_n \cos n\omega t) + \gamma k^T \cdot \Delta T_{\text{air}}(t) \\ &\quad + \{T_{\text{air}}(t) - (T_{0\_air} + A_{\text{air}} \cdot \sin(\omega t + \theta_{\text{air}}))\} \cdot \sum_{m=1}^M \gamma_m \cdot k_m \end{aligned} \quad (5)$$

Here,  $M$  represents the number of incorporated meteorological and surface factors;  $k_m$  and  $\gamma_m$  are the incorporated control and its associated multiplier; and  $\psi_1$  denotes the revised function between  $\gamma \Delta T_{\text{air}}$  and  $t$ . From Eq. (5), one can infer that the number of parameters is  $1 + 2N + M$ , indicating that at minimum LST observations of such a number are needed to solve the ATCF. The ATCF can potentially achieve a high degree of accuracy when the number of LST observations used as inputs is sufficiently large (substantially larger than  $1 + 2N + M$ ). However, the addition of more parameters results in a greater chance of over-fitting the problem and increasing the model complexity (Brooks et al., 2012), and in addition the number of LST observations within an annual cycle may be limited in practice (Wongsai et al., 2017). Hence, the ATCF should be simplified for practical use and the modeling of LST dynamics should consider both the prediction accuracy and the generalization ability.

### 3.2. Achieving a compromise in ATC modeling: balancing prediction accuracy and generalization ability

#### 3.2.1. Model formation

To balance the prediction accuracy and generalization ability, two issues should be considered: First, the number of harmonic functions in the ATCF needs to be constrained to maintain the generalization ability and to avoid the over-fitting problem, especially where data gaps are frequent (Brooks et al., 2012). In this study, we assigned the number of harmonics (i.e.,  $N$ ) to two (Fu and Weng, 2015; Bechtel and Sismanidis, 2017). Second, the number of the  $\Delta T_{\text{air}}$ -related controls (i.e.,  $M$ ) should also be constrained. Besides the SAT, four commonly used controls ( $M = 4$ ) were selected; they comprise the surface features NDVI, SM, and ALB, and the meteorological variable RH. We chose these controls because they are all closely related to the surface energy fluxes and therefore they regulate the  $\Delta T_{\text{air}}$ , as demonstrated in previous studies (Lin et al., 2016; Zhang et al., 2016; Benali et al., 2012). We are aware that additional factors may control the  $\Delta T_{\text{air}}$ , such as the impervious surface fraction, precipitation and wind velocity. Nevertheless, these factors either are already closely related to the four selected controls (Li et al., 2018b; Nojarov, 2012; Zhang et al., 2016), or they are relatively difficult to obtain in practice (Benali et al., 2012). Based on the abovementioned settings and the ATCF given by Eq. (5), we derived a

hybrid ATC model (hereafter termed the ATCH), expressed as follows:

$$\begin{cases} T_s(t) = T_0 + \sum_{n=1}^2 (a_n \sin n\omega t + b_n \cos n\omega t) + \gamma k^T \cdot \Delta T_{\text{air}}(t) \\ \gamma = (\gamma_1, \gamma_2, \gamma_3, \gamma_4); k = (k_1, k_2, k_3, k_4) \end{cases} \quad (6)$$

Here,  $\gamma_1$  to  $\gamma_4$  are respectively the daily NDVI, soil moisture, albedo, and relative humidity; and  $k_1$  to  $k_4$  are the associated multipliers. As expressed in Eq. (6), there are nine free parameters for the ATCH ( $T_0$ ,  $a_1$ ,  $a_2$ ,  $b_1$ ,  $b_2$ ,  $k_1$ ,  $k_2$ ,  $k_3$ , and  $k_4$ ), indicating that at least nine LST observations are required to solve the ATCH.

The following issues are noteworthy: First, the parameter number of the ATCH can still be too large for annual modeling with LSTs from polar-orbiting satellites that have a relatively narrow swath (e.g., Landsat observations). Further parameter-reduction approaches (PRAs) are therefore required to fit the modeling of such types of LST data. Further discussion of the possible PRAs based on the ATCH is provided in Section 5.1. Second, in principle, we can reduce the number of parameters of the ATCH from nine to eight, and even to three, in decreasing order, which results in six ATCH-based derivatives. These ATCH derivatives can be perceived as generalizations of several previous ATC models. For example, the ATCH approximates the ATCT given in Bechtel and Sismanidis (2017) once the parameters  $k_1$  to  $k_4$  are set as zero; it approaches the ATCE proposed by Zou et al. (2018) when  $a_2$ ,  $b_2$ ,  $k_2$ ,  $k_3$ , and  $k_4$  are set to zero; and it becomes equal to the ATCO when all the parameters except  $T_0$ ,  $a_1$ , and  $b_1$  are set to zero. The differences between the aforementioned ATC models are provided in Appendix A.

#### 3.2.2. Solution strategy

The nonlinear least square method was used to solve the free parameters of the ATCH. The initial values of the free parameters (including  $T_0$ ,  $a_1$ ,  $a_2$ ,  $b_1$ ,  $b_2$ ,  $k_1$ ,  $k_2$ ,  $k_3$ , and  $k_4$ ) were obtained using the first optimization software (1stOpt) due to its flexibility in determining initial values for nonlinear regression (Lin, 2011). In total, we selected 2479 MODIS pixels that cover sufficient varieties of land cover type and background climate. For each selected pixel with the 1stOpt, we applied an independent nonlinear regression to all the valid LSTs within an annual cycle in order to solve the free parameters. We then calculated the means of the resolved free parameters values derived from all the selected pixels as the initial values. Similarly, we employed the maxima and minima from all the selected pixels as the upper and lower bounds, respectively. After these procedures, the initial values of  $T_0$ ,  $a_1$ ,  $a_2$ ,  $b_1$ ,  $b_2$ ,  $k_1$ ,  $k_2$ ,  $k_3$ , and  $k_4$  were set as 293.1, 25.5, 3.6, 2.8, -3.1, 1.3, 0.2, -0.2, and 2.1, respectively, and parts of these initial values are comparable to those given by Bechtel (2012). Note that the nonlinear regression was subsequently conducted using Python 3.4, rather than directly based on the 1stOpt, mostly because of the difficulty in image

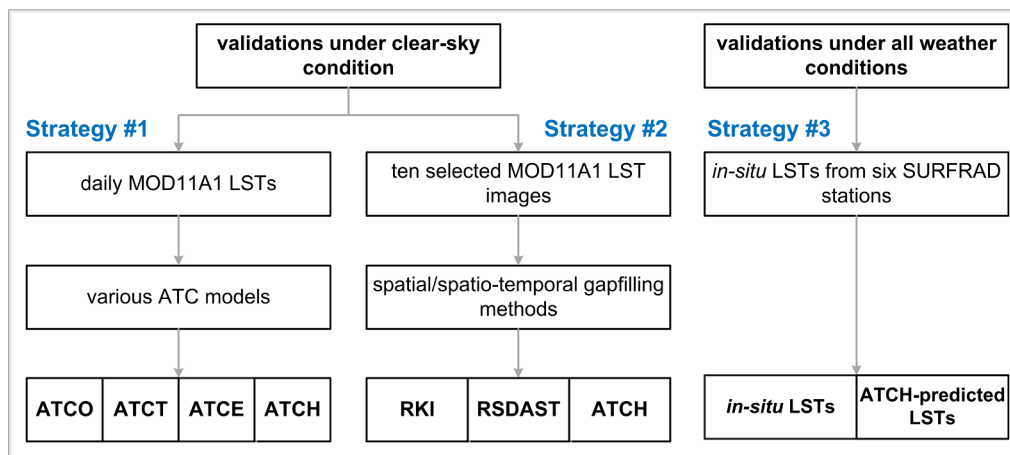


**Fig. 2.** Illustration of the three strategies used for evaluating the ATCH with MOD11A1 LSTs and *in-situ* LSTs. *Strategy #1* compares the ATCH with ATCO, ATCT, and ATCE using the MOD11A1 LSTs. In *Strategy #2*, 24 data gaps were preset for each selected image to assist the evaluation. The acronyms RKI and RSDAST represent the Regression Kriging Interpolation (RKI) method (Ke et al., 2013) and the Remotely Sensed DAily land Surface Temperature reconstruction (RSDAST) method (Sun et al., 2017), respectively. *Strategy #3* compares the results predicted by the ATCH (ATCH-predicted LSTs) with the *in-situ* LSTs under all weather conditions (i.e., including clear-sky and overcast).

batch processing for the latter tool. For each pixel, the aforementioned initial values, along with the valid LST observations as well as their associated DOYs within an annual cycle, were used to help solve the parameters of the ATCH using the least square method, with which the LST gaps were reconstructed.

### 3.3. Evaluation strategies

Three strategies were employed to evaluate the performance of the ATCH under clear-sky and all-weather conditions (Fig. 2). For clear-sky conditions, the performance of the ATCH was compared with other frequently-used ATC models (*Strategy #1*) and two gap-filling methods (*Strategy #2*). For all weather conditions (i.e., clear-sky and overcast conditions), the LSTs modelled by the ATCH were evaluated using the original *in-situ* LST data (*Strategy #3*).

*Strategy #1:* This strategy first compared the ATCH with the ATCO from both the spatial and temporal perspectives (see Section 4.1). To further compare the ATCH with all its possible derivatives, including the ATCT (Bechtel and Sismanidis, 2017) and ATCE (Zou et al., 2018), we quantified the contributions of several individual procedures to the improvement in accuracy with reference to the ATCO (see Section 4.1.2), using the attribution approach of Murray and Conner (2009). These procedures include the incorporation of additional harmonic functions (see ATCT), SAT and NDVI (see ATCE), SM, ALB, and RH. Comparisons using this strategy were conducted for all the available MOD11A1 LSTs over mainland China.

*Strategy #2:* The second strategy compared the ATCH with two recently proposed gap-filling methods, i.e., Regression Kriging Interpolation (RKI) (Ke et al., 2013) and Remotely Sensed DAily land Surface Temperature reconstruction (RSDAST) (Sun et al., 2017). We selected RKI and RSDAST as reference methods because they respectively represent spatial and spatio-temporal gap-filling methods. The comparisons were conducted over 10 selected days in 2012 (every 30 days starting from January 1, 2012), with the LST images derived from the MOD11A1 product. We chose the pixel in Row 2000 and Column 2000 of the MOD11A1 product over mainland China, and further employed it as the upper left corner to create 24 square data gaps on each LST image for the 10 selected days. These data gaps were labelled as the G01 to G24, with varying sizes including 1 × 1, 2 × 2, 3 × 3, 4 × 4, 5 × 5, 6 × 6, 7 × 7, 8 × 8, 9 × 9, 10 × 10, 20 × 20, 30 × 30, 40 × 40, 50 × 50, 60 × 60, 70 × 70, 80 × 80, 90 × 90, 100 × 100, 200 × 200, 300 × 300, 400 × 400, 500 × 500, and 600 × 600 pixels, respectively. We performed the same operation for all the selected 10 days of satellite images. The predicted LSTs over the data gaps using the ATCH or those gap-filling methods were then compared with the original LST values, based on which model performances were finally assessed.

*Strategy #3:* The third strategy applied the ATCH to *in-situ* LSTs from SURFRAD sites. The *in-situ* clear and overcast LSTs were identified by the MODIS pixels corresponding to the SURFRAD sites: i.e., we defined an overcast pixel as one in which the MODIS pixel was invalid data. The ATCH-predicted results were then compared with the *in-situ* LSTs under clear-sky, overcast, and all-weather conditions.

The absolute root mean-square error (RMSE) between the model predicted and observed LSTs was used to evaluate model performances. Specifically, we computed the RMSE difference between two methods (termed Drmse) to further evaluate the model performances from the spatial perspective in *Strategy #1*.

## 4. Results

### 4.1. Strategy #1: evaluation with previous ATC models

#### 4.1.1. Spatial and temporal patterns of ATCH performance

The spatial patterns of the performances of the ATCH and ATCO as well as their differences (given by Drmse) over mainland China is

illustrated in Fig. 3. Here, we mainly focus on the ATCH and ATCO; further details in terms of the ATCE and ATCT are presented in Section 4.1.2. The results show that the regional mean RMSEs for the ATCH during daytime and nighttime are 3.4 and 2.8 K, respectively, which are both significantly lower than those for the ATCO (i.e., 5.2 and 3.5 K during daytime and nighttime, respectively). These results also demonstrate that the RMSEs for both the ATCH and ATCO are higher in daytime than at nighttime, which is simply because the day-to-day LST variations during daytime are greater (Zou et al., 2018). The RMSEs of both the ATCH and ATCO are slightly lower in eastern and southeastern China than those in other areas, which may be because of the vegetation cover - since bare soil and low-density vegetation result in high LST fluctuations, while dense vegetation results in greater transpiration and cools the surface (Lin et al., 2016). In addition, LST and SAT are often well coupled over areas with densely vegetated canopies (Good, 2016) and with high soil moisture content (Mildrexler et al., 2011). Additionally, the ATCO shows slightly lower accuracies during daytime and nighttime in parts of the Qinghai-Tibet Plateau. This may be because LSTs in these mountainous regions often fluctuate dramatically due to complex climatic conditions and topography (Lin et al., 2016), which destabilize the regular ATC dynamics. The comparably high modeling errors of ATCH in these areas are probably related to inaccuracy in SATs interpolated across sparsely distributed stations.

To illustrate the improvements in accuracy of the ATCH when referenced to the ATCO response to land cover type, we provide the Drmse between these two models per land cover type (Fig. 4). In general, greater improvements in accuracy occur in more densely vegetated areas, whereas lower improvements occur in areas with less vegetation. Specifically, the Drmse for daytime is highest over grassland, farmland, closed shrubland, and natural vegetation, with a mean value that exceeds 2.0 K; whereas it is less than 1.3 K over areas of snow and ice where vegetation is absent. During nighttime, the maximum Drmse occurs over farmland, savanna, and natural vegetation, while it is less than 0.6 K over areas of snow and ice cover and open shrubland, with relatively low vegetation density. We speculate that the slightly greater accuracy over urban and built-up areas is attributable to the increased accuracy of the interpolated SATs, because the stations located on or near urban and built-up areas are usually more densely distributed (Fig. 1).

The above results elucidate the spatial variations of the performance of the ATCH. The temporal (daily scale) variations of the RMSEs predicted using the ATCH and ATCO are provided for three randomly selected pixels as examples (see Fig. 5). The associated comparisons demonstrate that, by incorporating information on daily variations from meteorological and surface data, the ATCH reliably depicts detailed fluctuations in LST within short intervals. Detailed scrutiny reveals that, with the ATCO, the LSTs were substantially underestimated between DOY (day of year) 90 and 150 and between DOY 250 and 340 (Fig. 5a1 and 5a2); whereas they were substantially overestimated between DOY 190 and 240 and between DOY 290 and 360 (Fig. 5b1 and 5c1). By comparison, the LSTs predicted using the ATCH generally agree well with the original LST observations and their associated variations. Similar results also occur during nighttime: e.g., LSTs were underestimated by the ATCO between DOY 80 and 130 (Fig. 5d1), although with different magnitudes.

In addition, the reconstructed daytime gap-free LST images by the ATCH on 15th of each month in 2012 were also produced to reveal changes in the spatiotemporal patterns (Fig. 6a-l).

#### 4.1.2. Sources of accuracy improvement

The specific contributions of all the additional procedures used by the ATCH when referenced to the ATCO on accuracy improvements are provided in Fig. 7. These procedures include the incorporation of the additional sinusoidal function (ASF), SAT, NDVI, SM, ALB, and RH.

The assessments demonstrate that the addition of SAT contributes the most to the ATCH, with a relative accuracy contribution of more

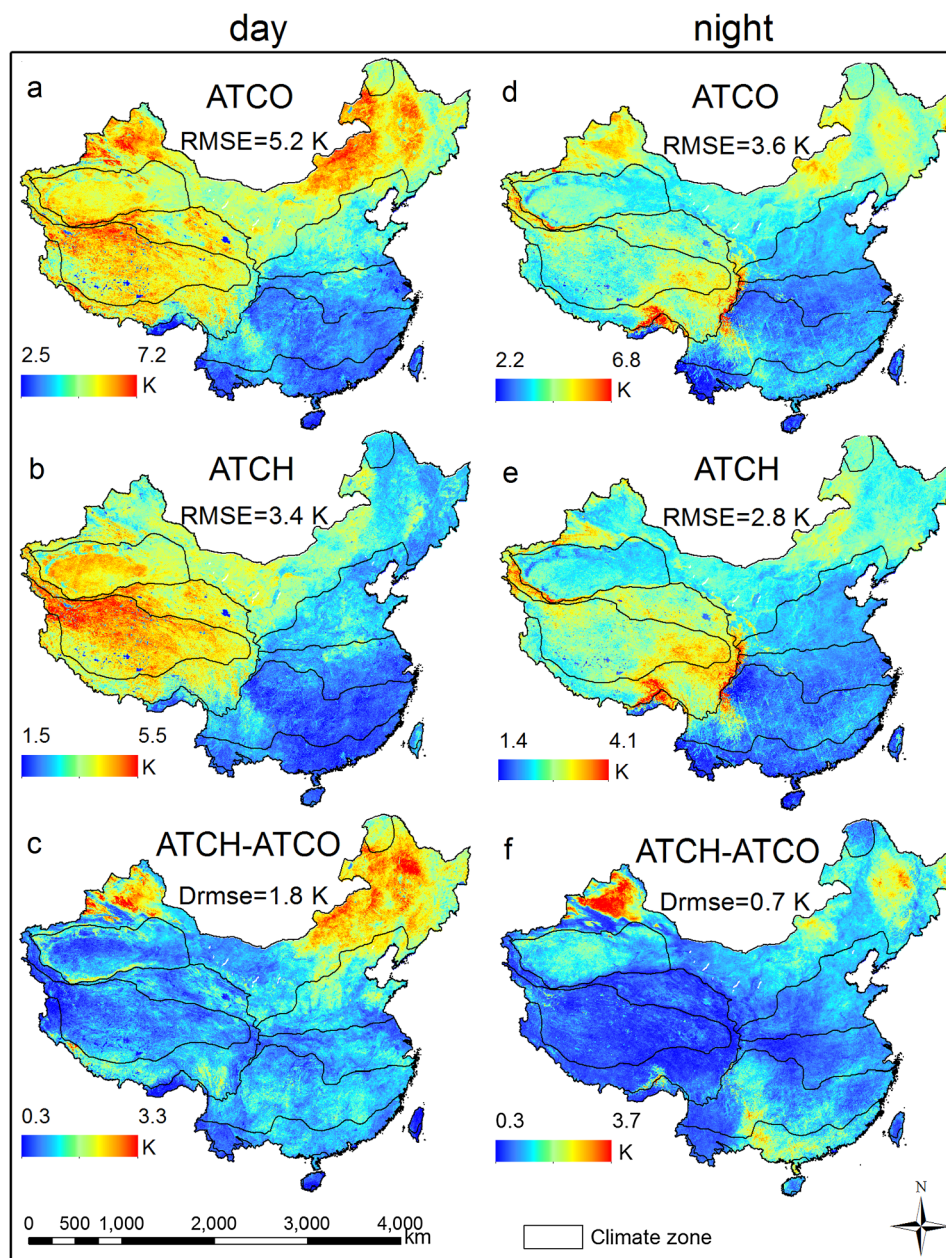


**Fig. 3.** Spatial variations of the RMSEs of the ATCH and ATCO models and the associated differences (Drmse) during daytime (the first column, a–c) and nighttime (the second column, d–f) based on all the available MOD11A1 LSTs in 2012.

than 40% for both daytime and nighttime. The incorporation of ASF results in the greatest degree of improvement: its contribution is around 16%, and the improvement is slightly greater at nighttime than during daytime. The incorporation of NDVI results in the third-greatest improvement, with the contribution of ~15% for both daytime and nighttime. The contributions due to the incorporation of SM, ALB, and RH are less significant compared with the previous three factors, with contributions of ~10%. Owing to the simultaneous increase or decrease across days, it is reasonable to conclude that the addition of SAT is the most important. Also, it is interesting that the combined incorporation of the NDVI, SM, ALB, and RH contributes more than 40% to the improvement in accuracy. This is mainly because the LST-SAT differences are modulated by relative humidity and the local surface status, including vegetation conditions (represented by the NDVI), soil moisture, and albedo (Good, 2016; Yang et al., 2017; Benali et al., 2012; Jin and Mullens, 2014).

As explained in Section 3, the incorporation of ASF can be regarded

as equivalent to the ATCT proposed by Bechtel and Sismanidis (2017), whereas the integration of the SAT and NDVI is comparable to the ATCE by Zou et al. (2018). Combining the strategies used by the ATCT and ATCE, as well as the additional incorporation of the SM, ALB, and RH, results in the ATCH performing better than both the ATCT (i.e., 4.4 and 3.4 K during daytime and nighttime, respectively) and ATCE (i.e., 4.2 and 3.1 K during daytime and nighttime, respectively). Notably, the contributions of individual factors, as shown in Fig. 7, are also potentially useful in applications in which the number of LST observations within an annual cycle is less than nine, in which case strategies should be designed to reduce the number of parameters of the ATCH, while simultaneously maintaining modelling accuracy. Further discussion of the PRA is given in Section 5.1.

The spatial variations of the contributions of individual factors to the improvements in accuracy are illustrated in Fig. 8. For the SAT, NDVI, SM, and RH, the greatest contributions occur in eastern and southeastern China, whereas smaller contributions occur in

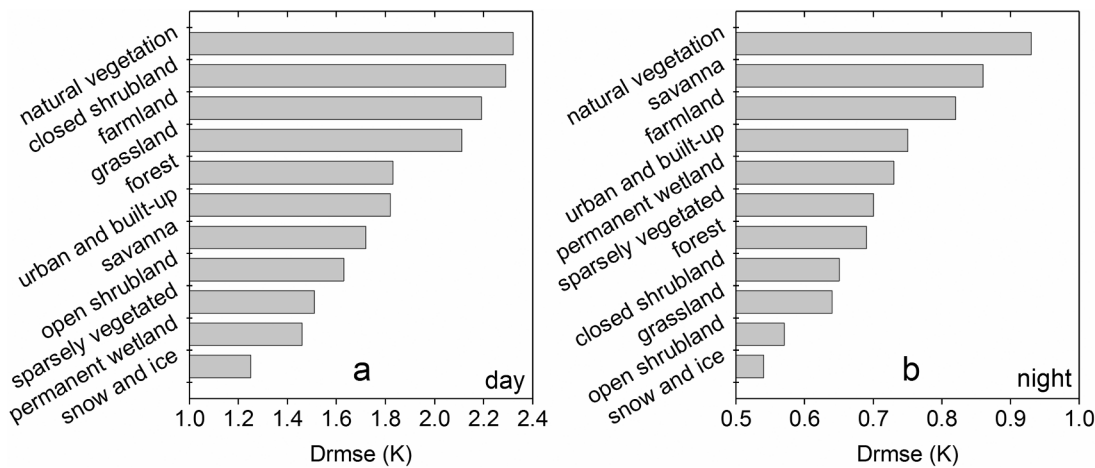


Fig. 4. Improvements in accuracy (i.e., the Drmse) of the ATCH with reference to the ATCO for different land cover types during daytime (a) and nighttime (b).

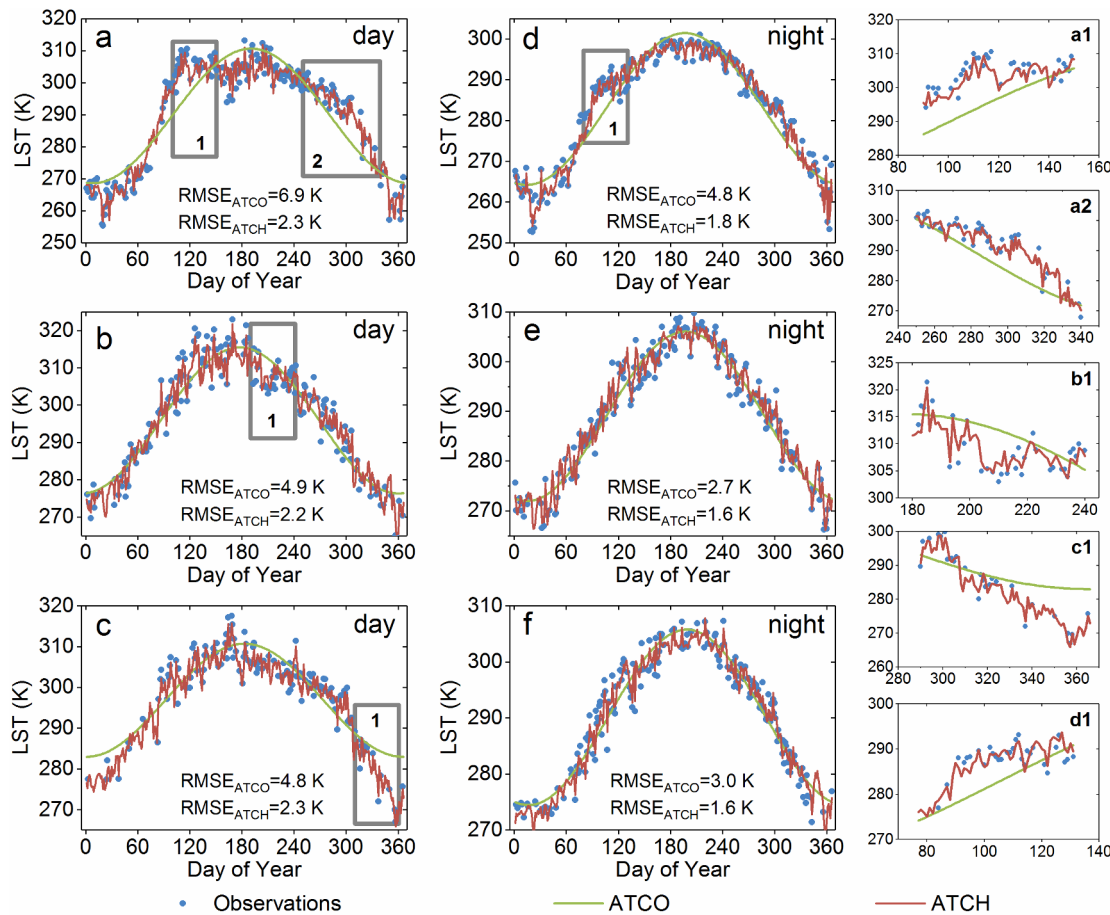
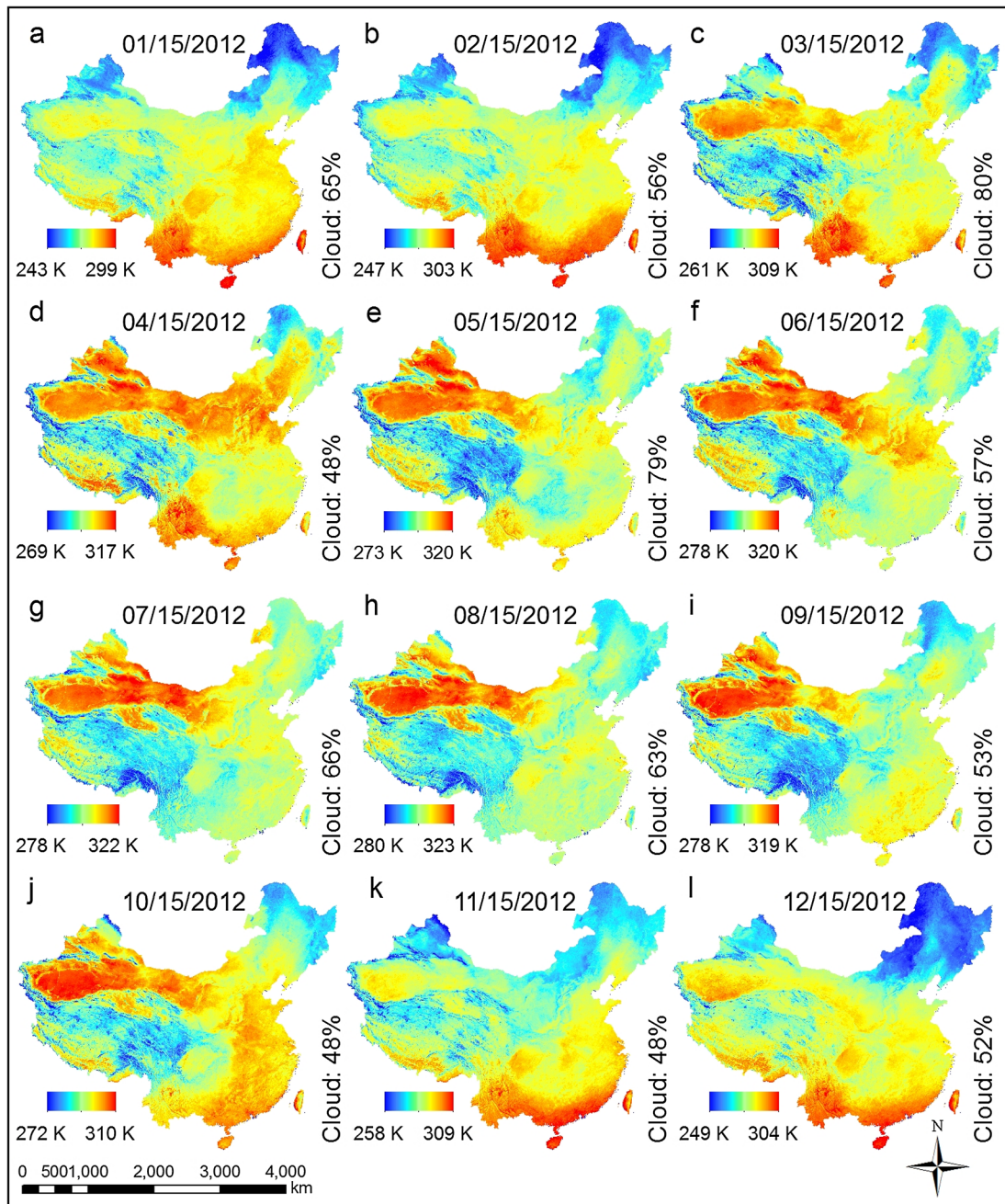


Fig. 5. Comparison of the model performances of the ATCH and ATCO at the daily scale at three randomly chosen pixels in daytime (the first column, from a–c) and nighttime (the second column, d–f). (a1), (a2), (b1), (c1), and (d1) shown in the third column show enlargements of the rectangles within the corresponding subfigures from the first and second columns. The RMSE<sub>ATCO</sub> and RMSE<sub>ATCH</sub> represent the errors by the ATCO and ATCH, respectively.

northwestern China; in contrast, for the ASF and ALB, greater contributions occur in northwestern China. These results can primarily be attributed to the fact that LST fluctuations are mainly influenced by vegetation status, precipitation (reflected by RH), and soil moisture (Good, 2016) across southeastern China which has a generally low elevation; whereas in northwestern China, the surface of which is generally sparsely vegetated or bare soil, LST fluctuations are affected

more by the albedo (Mildrexler et al., 2011). Notably, larger errors in LST retrieval over bare soil may also contribute to the slightly higher contribution of the ASF across northwestern China. In addition, it is noteworthy that there is no significant difference in contribution between daytime and nighttime. Several discrepancies between daytime and nighttime may be ascribed to surface properties or to diurnal changes in weather.



**Fig. 6.** The reconstructed MODIS LSTs during the day in 2012. Only LST images on 15th of each month are listed (a-l). The value subsequent to the ‘Cloud’ denotes the cloud cover percentage for each month over mainland China.

#### 4.2. Strategy #2: Performance comparison with other statistical gap-filling methods

The comparisons between the ATCH and two frequently used gap-filling methods (i.e., RKI and RSDAST) are illustrated in Fig. 9. In general, the evaluations reveal that, although with a slight trend of increasing modelling error, the performances of the ATCH and RKI remain relatively stable with increasing gap size. By contrast, the performance of the RSDAST decreases progressively with increasing gap size. Notably, the mean RMSE of ATCH is always lower than that of the RKI over modelled gap sizes. This is understandable because the RKI is based on a linear relationship between the clear-sky LSTs and the two key variables including the NDVI and elevation, with which the LST gaps can then be reconstructed. In other words, the RKI assumes that the variations of the NDVI and elevation are fully capable of explaining

those of LSTs. This assumption may be applicable in most cases, but it is not sufficiently accurate for predicting LSTs because other factors, such as soil moisture and especially synoptic conditions, are also responsible for a large proportion of the LST variations (Sandholt et al., 2002).

A different phenomenon was observed for the RSDAST. The assessments indicate that the RSDAST achieves a better performance than the ATCH when the LST gap size is small; however, the performance of RSDAST is worse than that of ATCH when the gap size gradually increases and exceeds G19 ( $100 \times 100$  pixels) (see Fig. 9). The better performance of the RSDAST when compared with the ATCH with a small gap size is probably because the RSDAST is based on ‘spatio-temporal’ interpolation: i.e., the spatial correlations among adjacent pixels have been incorporated in the gap-filling process in addition to the interpolation of temporally discontinuous LSTs (Pede and Mountrakis, 2018). This better performance may also be because the

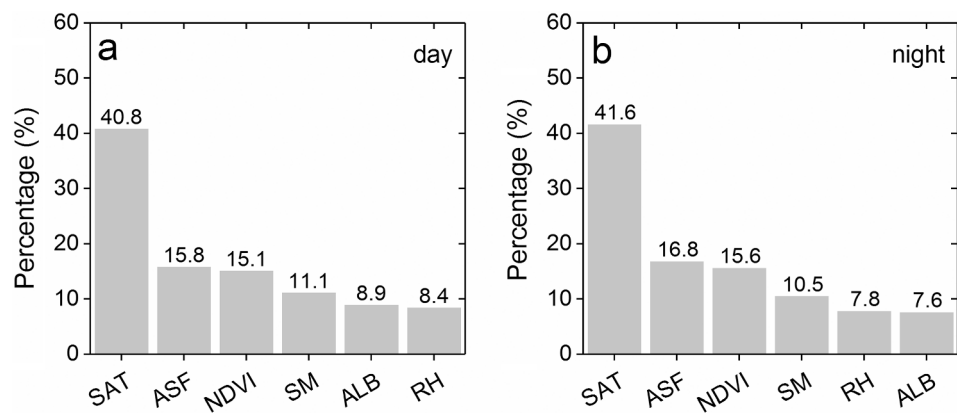


**Fig. 7.** Mean contributions of accuracy improvements (in percentages, %) using the SAT, ASF, NDVI, SM, ALB, and RH for daytime (a) and nighttime (b) across mainland China.

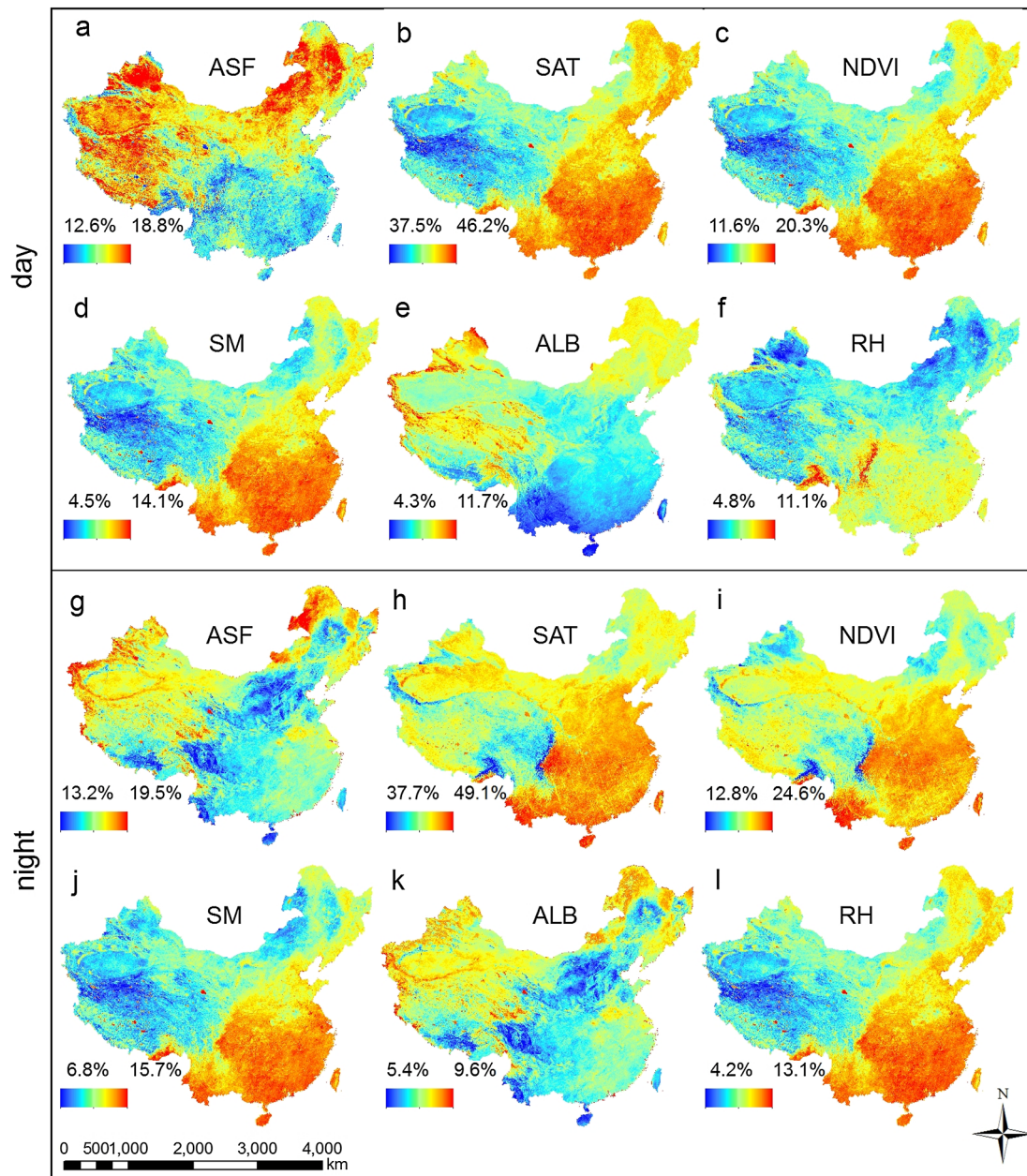


**Fig. 8.** Spatial variations of the contributions to accuracy improvement (in percentages, %) by incorporating SAT, ASF, NDVI, SM, ALB, and RH for daytime (first and second rows, a-f) and nighttime (third and fourth rows, g-l).

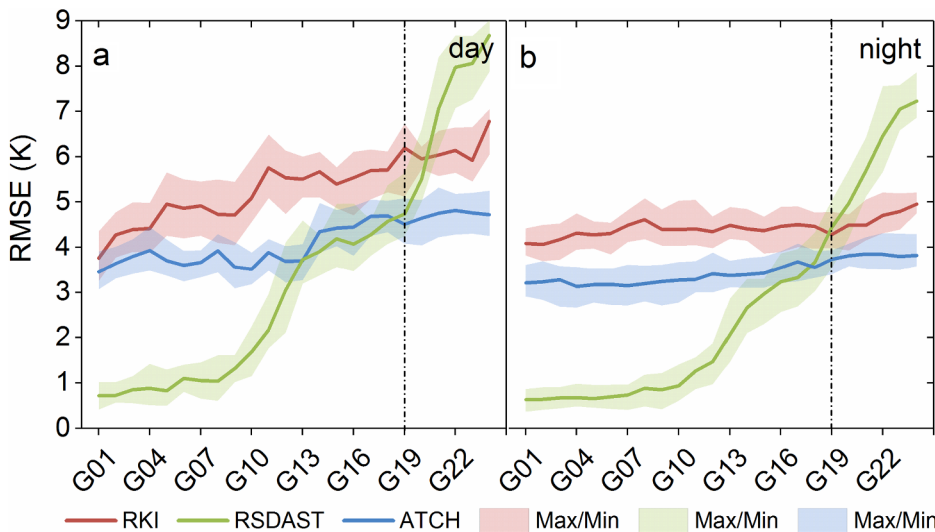


**Fig. 9.** Performance comparisons between the ATCH and two frequently-used gap-filling methods, namely RKI and RSDAST, for daytime (a) and nighttime (b). G01 to G24 denote the 24 LST gaps with gradually increasing sizes (from  $1 \times 1$  to  $600 \times 600$  pixels), with the specific values given in Section 4. The solid lines and associated rectangular boxes represent the mean RMSE and the maximum/minimum RMSE. The vertical dashed lines indicate the gap size (i.e., G19:  $100 \times 100$  pixels) for which the performances of the three models are similar.

RSDAST employs spatiotemporally local information to assist in the LST interpolation. It is reasonable that the ‘spatiotemporal’ and ‘local’ nature of a model (e.g., the RSDAST) would make it especially appropriate for interpolations wherein the spatial (temporal) gap size is small (narrow). Similarly, such spatiotemporal methods would become less effective, and even unfeasible, when the spatial (temporal) gap size becomes large (long). This is because spatiotemporally local information in this scenario is unable to help interpolate large data gaps around which there are no (or very few) valid pixels. The decreasing performance with increasing gap size is confirmed by Fig. 9, which shows that the prediction error of the RSDAST can reach approximately 9.0 K when the gap size reaches  $600 \times 600$  pixels. Furthermore, the spatiotemporal models build a ‘local’ regression relation for each pixel, and thus the generalization ability is relatively low. By incorporating a ‘global’ (corresponding to the ‘local’ nature of most gap-filling methods) regression strategy and physical background (e.g., the use of SAT), the ATCH may not be the best choice when the gap size is small, but its performance can be maintained even if the data gaps become very large. We also fully acknowledge that an even better spatiotemporal model for interpolating LSTs can be designed when the advantages of the ATCH and RSDAST are combined. Further discussion of the further development and applications of ATC models is provided in Section 5.2.

#### 4.3. Strategy #3: assessment of the modelled LSTs under all-weather conditions

The performances of the ATCH with reference to *in-situ* measurements under all-weather conditions (including both clear and overcast sky) are provided in Table 5. The assessments show that the LSTs modelled using the ATCH generally agree well with the ground-based

measurements, with mean RMSEs of 2.7 and 2.1 K for daytime and nighttime, respectively. Specifically, the RMSEs are typically higher under overcast than under clear-sky conditions. For example, the mean RMSEs for daytime and nighttime under clear-sky conditions are 1.9 and 2.0 K, respectively; whereas the values under overcast sky are 3.2 and 2.2 K, respectively. This contrast indicates a slightly lower competence of the ATCH for reconstructing LSTs under overcast conditions, suggesting that the procedure and auxiliary data incorporated (e.g., the ASF, SAT, and NDVI) are probably not sufficiently capable of describing the true LST dynamics under overcast sky conditions.

To achieve an in-depth comparison of the ATCH performances over the clear- and overcast sky pixels at the daily scale, we derived the daily true LST dynamics obtained from the SURFRAD sites and the results reconstructed by the ATCH. Three sites were chosen as examples and the comparisons are presented in Fig. 10. For all three sites, the evaluations indicate that the LSTs predicted using the ATCH generally agree well with the LST observations for clear-sky pixels. For overcast pixels, the reconstructed LSTs are close to the measurements for nighttime, whereas they are mostly overestimated for daytime. This is probably because only clear-sky LSTs were used to drive the ATC modelling, although surface and meteorological information under overcast conditions (e.g., the SAT and RH) were also employed. The relationships between the LSTs and the associated factors obtained under clear-sky conditions become less capable of being used to predict LSTs for the overcast pixels. This reduction in accuracy is more pronounced for daytime than for nighttime, because the LST-SAT differences are greater for daytime due to daytime insolation (Good, 2016; Gallo et al., 2011).

The reduced accuracy for overcast situations accords with previous studies. The ATCH actually demonstrates several advantages over the

**Table 5**

Accuracies (represented by the RMSE; unit: K) of the reconstructed LSTs by the ATCH with reference to *in-situ* LSTs measured at the seven SURFRAD sites under clear-sky, overcast-sky, and all-weather conditions.

Site	RMSE for daytime (K)			RMSE for nighttime (K)		
	Clear-sky	Overcast-sky	All-weather	Clear-sky	Overcast-sky	All-weather
BON	1.6	3.0	2.5	2.0	2.0	2.0
BCO	2.3	3.6	3.1	2.4	2.7	2.5
FPK	2.7	3.3	3.1	2.1	2.3	2.2
GWN	1.3	3.5	2.6	1.4	1.8	1.6
PST	1.9	3.0	2.7	1.6	1.8	1.7
SXF	1.5	2.7	2.2	2.4	2.4	2.4
DRA	2.3	3.2	2.7	2.2	2.3	2.3
Mean	1.9	3.2	2.7	2.0	2.2	2.1

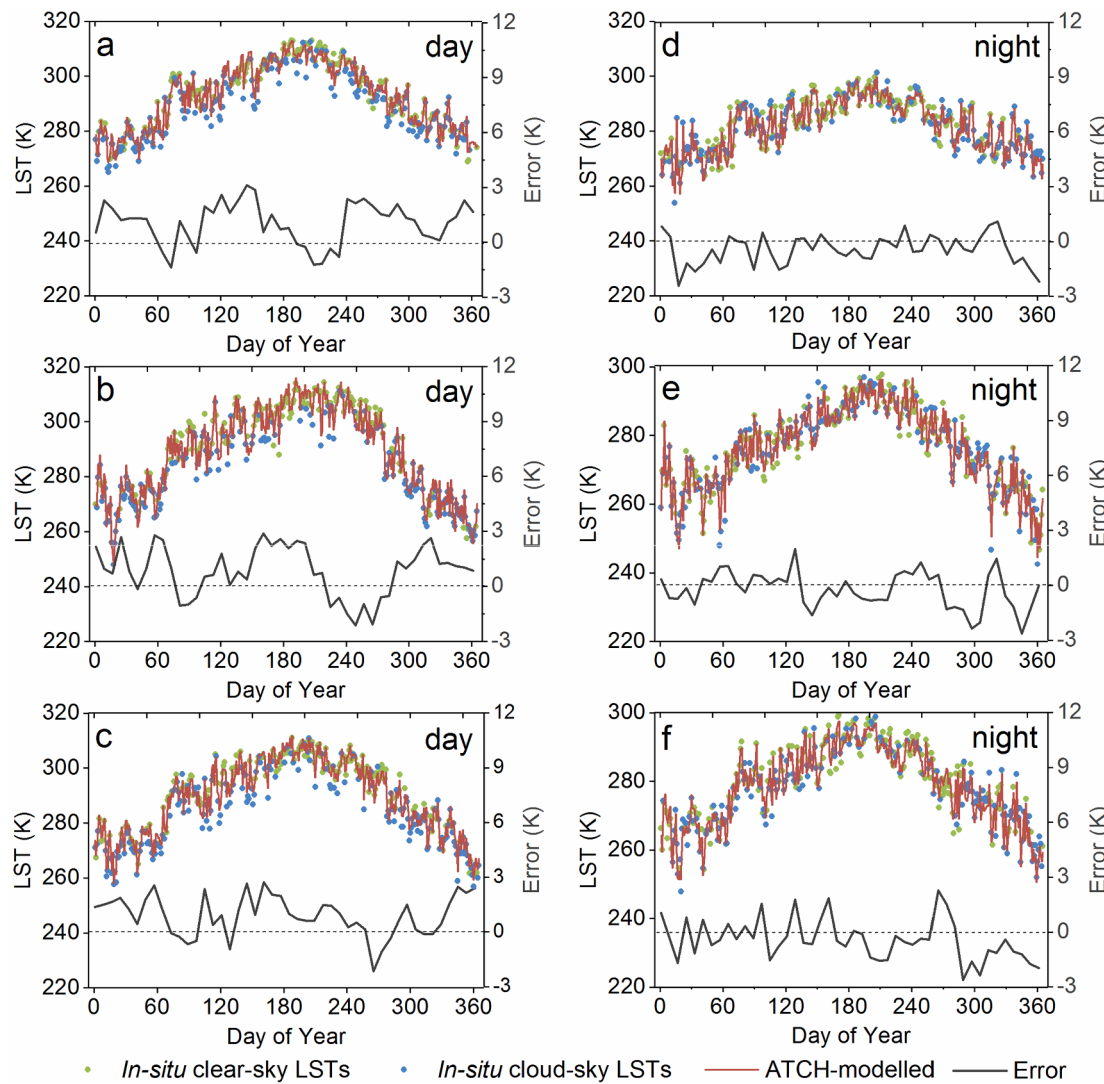


**Fig. 10.** Comparisons between the LSTs predicted using the ATCH and those measured at three SURFRAD sites (i.e., the BON, FPK, and SXF) for daytime (the first column) and nighttime (the second column). The ‘Error’ denotes the mean difference between the ATCH-predicted and *in-situ* LSTs at the 8-day scale. The surface types of BON, FPK and SXF are mostly grassland and cropland.

existing methods (Lu et al., 2011; Yu et al., 2014; Zeng et al., 2018): the overcast sky RMSEs predicted using the ATCH at these sites are only 2.7–3.6 K and 1.8–2.7 K for daytime and nighttime, respectively (Table 5). These errors are considerably lower than those in previous reports, which typically demonstrated that the mean RMSEs over overcast pixels are approximately 4.5 and 3.5 K for daytime and nighttime, respectively. This modification implies that the SAT and RH contain information about LST variations under overcast conditions.

## 5. Discussion

### 5.1. Parameter-reduction approaches (PRAs) for the ATCH

The ATCH with nine free parameters was shown to have a generally high accuracy and well-behaved generalization ability in deriving annual LST dynamics. Note that practitioners may need to model the annual LST dynamics under scenarios where the number of input LSTs is less than nine, e.g., the number of valid Landsat thermal observations (with the 16-day revisit frequency) within an annual cycle may be fewer than nine in some subtropical or tropical areas where clouds are prevalent. Based on the analysis of the model structure and the attribution of contribution to accuracy improvements, we therefore

proposed different PRAs to reduce further the parameter number of the ATCH to less than nine, aiming to formulate model derivatives that are able to adapt different scenarios. Over regions that experience severe cloudy conditions (i.e., the number of valid LST observations may be less than nine), the ATCH-derivatives with less parameters remain usable to assist the generation of daily LSTs with fine spatial and temporal resolutions (Weng et al., 2014; Fu and Weng, 2016) or the examination of landscape thermal patterns (Bechtel, 2011; Fu and Weng, 2015).

The parameter reduction was generally conducted by setting a portion of the parameters of the ATCH to zero and the orders of parameter-reduction were based on the contributions to accuracy improvements provided in Section 4.1.2. Using Case 4 as an example, the PRA ‘ $k_2, k_3$ , and  $k_4 = 0$ ’ indicates that these three parameters are preset to zero (i.e., remove the  $k_2\gamma_2$ ,  $k_3\gamma_3$ , and  $k_4\gamma_4$  in Eq. (6)) and accordingly only six parameters are left (i.e.,  $T_0$ ,  $a_1$ ,  $b_1$ , and  $k_1$ ). Similarly, under Case 2, the PRA ‘ $k_4 = 0$ ’ used for daytime differs from that for nighttime ( $k_3 = 0$ ). This is because the abovementioned attributions specify that the RH (its multiplier is  $k_4$ ) is the least important factor contributing to accuracy improvements, whereas the albedo (its multiplier is  $k_3$ ) was specified to play such a role for nighttime. From these PRAs, we finally obtained six ATCH-based derivatives (corresponding to Cases 2 to 7),

**Table 6**

Model derivatives obtained from the original ATCH with different PRAs as well as the associated performances (denoted by the RMSE in unit K).

Cases	Number of parameters	PRAs*	RMSE		Model derivatives
			Day	Night	
Case 1	9	—	3.4	2.8	ATCH
Case 2	8	$k_4 = 0$ (day) or $k_3 = 0$ (night)	3.6	2.9	—
Case 3	7	$k_3$ and $k_4 = 0$	3.7	2.9	—
Case 4	6	$k_2$ , $k_3$ , and $k_4 = 0$	3.9	3.0	ATCH_C4
Case 5	5	$a_2$ , $b_2$ , $k_3$ , and $k_4 = 0$	4.0	3.0	ATCH_C5
Case 6	4	$a_2$ , $b_2$ , $k_2$ , $k_3$ , and $k_4 = 0$	4.2	3.1	ATCE
Case 7	3	$a_2$ , $b_2$ , $k_1$ , $k_2$ , $k_3$ , and $k_4 = 0$	5.2	3.5	ATCO

\*  $T_0$ ,  $a_1$ ,  $a_2$ ,  $b_1$ ,  $b_2$ ,  $k_1$ ,  $k_2$ ,  $k_3$ , and  $k_4$  are the nine free parameters of the ATCH (see Eq. (6)). Note that under Case 2, the PRAs used for the daytime and nighttime are different: the PRA ' $k_4 = 0$ ' was used for daytime and the PRA ' $k_3 = 0$ ' was used for nighttime. The column 'Model derivatives' only lists the optimal ATCH-based derivatives for each case.

with the parameter number ranging from eight to three, in decreasing order (see Table 6). Note that the derived model under Case 6 is approximately equivalent to the ATCE proposed by Zou et al. (2018); and that under Case 7 it is equal to the ATCO of Bechtel (2011). All the derived models were then used to reconstruct the LSTs over mainland China, and the associated RMSEs of each model are listed in Table 6. These results show that the prediction errors of the ATCH-derivatives increase gradually with decreasing parameter number, with the RMSE rising from 3.4 (2.8) to 5.2 K (3.5 K) for daytime (nighttime). In contrast, the addition of more LST-related controls to the ATCH is anticipated to increase the prediction accuracy of LSTs, but this would result in ATCH-derivatives that are more sophisticated and therefore would probably decrease the generalization ability of the model. Further discussion related to the additional usable controls is given in Section 5.2.2. With these derivatives, practitioners have more options for choosing the most appropriate model for specific scenarios.

In addition, we need to clarify that the PRAs were proposed based on the empirical results presented above. There may exist alternatives, yet here we only choose the best one that balances the prediction accuracy and generalization ability. Using Case 4 as an example, instead of setting  $k_2$ ,  $k_3$ , and  $k_4 = 0$  (i.e., as indicated for the ATCH\_C4), we can also combine  $k_1$ - $k_4$  to one  $k$  while still keep  $\gamma_i$  ( $i = 1, 2, 3, 4$ ) in Eq. (6) to obtain a new ATCH-based derivative (here termed the ATCH\_SK) with six parameters. The ATCH\_SK requires incorporations of multiple factors including NDVI, soil moisture, albedo and relative humidity, which would likely decrease the model generalization ability when compared with the ATCH\_C4. Similarly, under Case 5, we recommend ATCH\_C5 because ATCH\_C5 behaves a higher accuracy than ATCT proposed by Bechtel and Sismanidis (2017).

## 5.2. Prospects and limitations

### 5.2.1. Prospects

By balancing prediction accuracy and generalization ability, this study proposes a hybrid framework (i.e., the ATCH) for modelling annual LST dynamics with satellite-derived LSTs as model inputs. The ATCH has been shown to possess a high degree of accuracy and it can derive a series of sub-models that are suitable for various scenarios with different numbers of input LST images within an annual cycle. The following points are noteworthy: (1) The ATCH is a 'global' framework, which indicates that for annual modeling all the LSTs within a year are used as inputs to drive the modeling simultaneously for each pixel. (2) The ATCH is formulated only from the temporal perspective, i.e., it is a 'temporal' framework and no adjacent spatial information was

incorporated during model formulation. The prediction accuracy of the ATCH will be improved by incorporating neighboring-pixel information if the generalization ability is ignored. (3) The ATCH is a 'semi-physical' framework, indicating that mechanisms of heat transfer have been incorporated in the modelling.

The 'global' and 'temporal' features guarantee its generalization ability, such that the associated model performance barely changes with the decreasing input number of LST images; however, they also result in reduced prediction accuracy compared to the spatiotemporal interpolation models when the LST gaps are spatially small or temporally narrow. This study was not intended to design a method/algorithim that is able to reconstruct LST gaps with the highest accuracy in all scenarios, although its performance when the LST gaps are large is promising. Rather, it primarily aims at providing a temporal modelling framework that is potentially valuable for designing better spatiotemporal models for interpolating LSTs. For example, the LST gaps may be reconstructed with an even higher degree of accuracy once spatially local information is integrated into the temporal modeling, such as demonstrated recently by Li et al. (2018a). The ATCH is also potentially useful for the spatiotemporal fusion of LST products with different resolutions, such as those conducted by Weng et al. (2014) and Quan et al. (2018). The 'semi-physical' nature of the ATCH makes it comparable to the very complex land surface models, which can simulate subsurface, surface, and atmospheric variables simultaneously in addition to the LST. In fact, the ATCO can be perceived as a simplified LSM, because it can be interpreted solely as the solution of the heat conduction equation when constrained by the surface energy balance, with insolation (which is generally sinusoidal within an annual cycle) as the major surface flux that drives the annual LST dynamics. Compared with the LSMs, the ATCH is much simpler and can be more suitable for the modeling of LST dynamics at a very high spatial resolution (e.g., 100 m for the Landsat thermal data, or even finer).

### 5.2.2. Limitations

Although progress has been made, there are several limitations of the ATCH that require attention in the future: First, the ATC modeling can be performed on either the daily mean LST or instantaneous LST at a fixed time within a diurnal cycle. Nevertheless, the overpass times for MODIS LST observations may vary slightly from day-to-day: e.g., the maximum difference in overpass time for the MODIS LSTs acquired in the morning within an annual cycle can reach 2.0 h. Prior to the ATC modelling, temporal normalization of LSTs is therefore needed to help adjust the daily LSTs to the same overpass times during a diurnal cycle. In this study, we performed a normalization of LSTs according to the approach proposed by Duan et al. (2014). The results provided in Appendix B indicate that the LST normalization procedure slightly improves the accuracy of ATC modelling. In addition, we used the daily mean SATs to assist the modeling. The ATC modeling may be further improved once instantaneous SATs shortly after the overpass times of MODIS observations are employed, considering the phase difference in timing (around 2 h) between the LST and SAT (Good, 2016). Furthermore, the resolutions of the additional datasets were resampled to 1 km to match that of the LST product, which may introduce uncertainties for analyzing the contributions to accuracy improvements. We therefore performed a comparison to investigate the scaling effect of accuracy assessments at the 1- and 25-km scales. The results indicate that the scale of these datasets only slightly affects the contributions to accuracy improvements, with the percentage of less than 0.5% for both the day and night. Likewise, because of the surface thermal anisotropy, the variations in view angles of observed LSTs (e.g. varying from  $-55^\circ$  to  $+55^\circ$  for the MODIS LSTs) can also induce uncertainties (Wan et al., 2002). Although the angular normalization of LSTs was achieved at the pixel scale in previous studies (Li et al., 2013), there is currently, to the best of our knowledge, no practical and simple way to perform an angular normalization for the MODIS LSTs.

Second, the ATCH has been shown to produce relatively higher

RMSEs over areas with less vegetation: e.g., over snow and ice. One possible reason may be because of the inaccurate SATs interpolated with very few *in-situ* SATs by the simple spatial interpolation method over these areas. Another possible reason is that the LST-related controls selected by this study are insufficient for representing the daily LST variations for these areas: for example, the LST-SAT relationship over snow-covered areas becomes weaker than that over snow-free areas (Shamir and Georgakakos, 2014). With a better method for interpolating SATs, such as that proposed by Zhang et al. (2016), and with the involvement of more factors directly or indirectly related to the LST, such as topography (Hengl et al., 2012) and the snow index (Shamir and Georgakakos, 2014), the performance of the ATCH model is anticipated to be further improved.

Third, despite the notable improvement in simulating overcast-sky LSTs when compared with previous methods that mainly focus on clear-sky conditions, the ATCH has been demonstrated to slightly overestimate LSTs under overcast conditions. This is probably because the incorporated meteorological and surface factors are still inadequate to reflect the LST variations under overcast sky. Previous studies have tried to incorporate additional data that has a more direct relationship with LSTs under overcast sky: such as microwave data (Duan et al., 2017; Kou et al., 2016), cloud properties (Aires et al., 2004; Fan et al., 2015), and especially surface radiation fluxes (Zhang et al., 2015; Zeng et al., 2018). For example, although uncertainties may exist regarding the incident shortwave radiation (ISR) product (Zhang et al., 2014), the ISR is anticipated to better reflect the impacts of cloud on the LST than the LST-related controls used in the present study. This is because the ISR generated by Zhang et al. (2014) was generated by considering the surface status and the sky conditions, and it is therefore highly desirable to integrate this related information to assist the ATC modeling under overcast conditions.

## 6. Conclusion

Annual temperature cycle (ATC) models have been found valuable for the generation of spatio-temporally seamless LSTs, as well as for various applications. However, current ATC models were developed with the emphasis either on prediction accuracy or on generalization ability; and they remain incapable of providing options for users in the adaptation to various scenarios when different numbers of thermal observations are available as model inputs. To overcome these limitations, we propose a flexible ATC modelling framework (termed the ATCF) by integrating multiple harmonics and a linear function of LST-related factors. Starting from the ATCF, we obtained a hybrid ATC model (termed the ATCH) that can balance prediction accuracy and generalization ability by combining two harmonic functions with a linear function of surface air temperature (SAT), NDVI, albedo, soil moisture, and relatively humidity. Based on the ATCH, various parameter-reduction approaches (PRAs) were designed to provide model derivatives when different numbers of thermal observations are available.

## Appendix A. Demonstration of two predetermined assumptions used for model construction

The first assumption is that '*an increased number of harmonics is required for modelling both the primary and subordinate components of the LST dynamics, but there exists a suitable number of harmonics to assist the modeling of the inter-annual LST dynamics stably*'. A comparison of the modeling capability among the ATCO (with a single harmonic) (Bechtel, 2011), ATCT (with two harmonics) (Bechtel and Sismanidis, 2017), and the HANTS (with a series of harmonics) (Xu and Shen, 2013) was presented in Fig. A1a. This comparison indicates that both the HANTS and ATCT achieve a better performance than the ATCO. The HANTS does simulate well some of the short-term LST variations, but the use of a large number of harmonics more than needed by the HANTS would probably render the associated ATC model unstable (e.g., the over- and under-fitting phenomena as shown in Fig. A1a1) (Brooks et al., 2012).

The second assumption is that '*meteorological (e.g., SATs) and surface and status can be used to help formulate an ATC model that is sufficiently stable as well as capable of representing daily LST fluctuations*'. Previous studies have integrated the SATs and surface status (i.e., the NDVI) to help model the daily LST fluctuations (Zou et al., 2018): Day-to-day SATs are strongly coupled with those in LSTs though with different magnitudes ( $\Delta T_{\text{air}}$ ) (Kloog et al., 2014; Good, 2016; Good et al., 2017); and  $\Delta T_{\text{air}}$  can be regulated by the NDVI to some extent. Our further analysis, illustrated by Fig. A2c and d, demonstrates that the differences between the observed and modeled SATs by Eq. (4) are similar to those on LSTs, with the correlation

Three strategies were employed to evaluate the ATCH under both clear- and overcast-sky conditions. The first and second strategy compared the ATCH with the original sinusoidal ATC model (termed the ATCO) and its variants, as well as with two gap-filling methods (i.e., the RKI and RSDAST) under clear-sky conditions. In the third strategy, the LSTs predicted by the ATCH were directly evaluated with *in-situ* LST measurements under both clear- and overcast-sky conditions. The assessments show that the ATCH has a greater accuracy than the ATCO, with decreased RMSEs of 1.8 and 0.7 K for daytime and nighttime, respectively. By comparing the ATCH with the RKI and RSDAST, we found that the ATCH performs better than the RKI and it also performs better than the RSDAST for large gap sizes (e.g., 100 × 100 pixels). This result implies that the ATCH has the advantage of filling spatially large and temporally long LST gaps, and thus it has a better generalization ability compared to most gap-filling methods. By incorporating LST-related factors under overcast conditions, the ATCH shows a better performance in filling LSTs under clouds than approaches that only incorporate information under clear-sky conditions. Further attribution analysis shows that the addition of a sinusoidal function (ASF), SAT, NDVI, and other LST-related factors can respectively contribute around 16%, 40%, 15%, and 30% to the improved accuracy. This analysis is useful for providing model-derivatives by PRAs designed. With these derivatives, practitioners will have more options for selecting the most appropriate model for specific scenarios. We believe that the ATCH can enhance the quality of LST products and extend the associated applications.

## Acknowledgements

We gratefully acknowledge NASA's Land Processes Distributed Active Archive Center (LP DAAC) for providing the MODIS product; a project funded by NASA's Earth Science Data Systems (ESDS) Program for the Earth Observing System Data and Information System (EOSDIS); and the China Geospatial Data Cloud for providing the L1 T Landsat images. We also thank the China Meteorological Administration National Satellite Meteorological Center (CMA NSMC) for provision of the *in-situ* observations.

This work is jointly supported by the Key Research and Development Programs for Global Change and Adaptation of China under Grant number 2016YFA0600201, the National Natural Science Foundation of China under Grant 41671420, the Jiangsu Provincial Natural Science Foundation under Grant number BK20180009, the Key Research and Development Programs for Global Change and Adaptation of China under Grant number 2017YFA0603604, and the Fundamental Research Funds for the Central Universities of China under Grant number 090414380017. We are also grateful for the financial support provided by the DengFeng Program-B of Nanjing University, and the financial support provided by the Cluster of Excellence 'CliSAP' (EXC177), University of Hamburg, funded through the German Science Foundation (DFG), Germany.

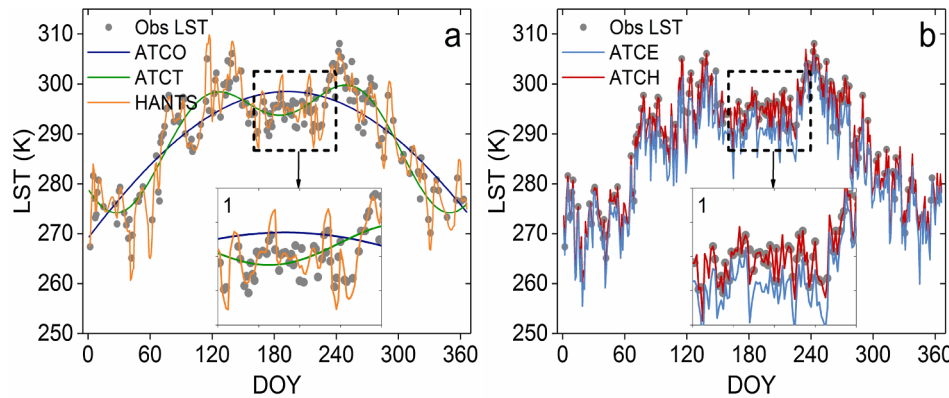


**Fig. A1.** A demonstration of the two predetermined assumptions used for model construction, wherein (a) and (b) are used for elucidation of the first and second assumptions, respectively. The Obs LST, ATCO, ATCT, and HANTS in (a) represent the observed LST dynamics and the predicted LSTs by incorporating a single sinusoidal function (Bechtel, 2011), two harmonics (Bechtel and Sismanidis, 2017), and a series of harmonics (Xu and Shen, 2013), respectively. The Obs LST, ATCE, and ATCH in (b) represent the observed LST dynamics and the predicted ones by the incorporations of SATs and NDVI (i.e., the ATCE) (Zou et al., 2018) and of more information on surface and meteorological status (i.e., the ATCH), respectively. (a1) and (b1) are two enlarged panels that illustrate the modeling details around DOY 200.

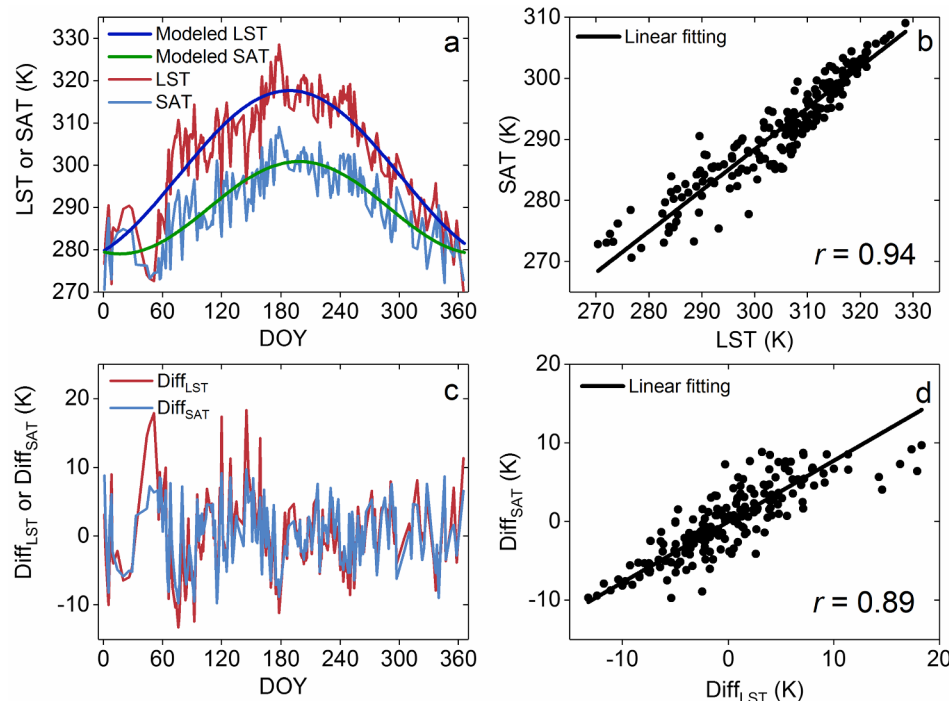


**Fig. A2.** A demonstration of the similarity between the LST and SAT dynamics as well as the similarity of the differences between the observed and modelled LSTs and SATs. (a) The observed daily LST and SAT dynamics for an entire year at a specific MODIS pixel where an *in-situ* site is located. (b) The correlations between the LSTs and SATs. (c) Diff<sub>LST</sub> and Diff<sub>SAT</sub> represent the differences between the observed and modelled LSTs and SATs for an entire year, respectively, again for the aforementioned specific pixel. (d) The correlations between Diff<sub>LST</sub> and Diff<sub>SAT</sub>.

**Table B1**

Modelling accuracy of the ATCH using the original MODIS LSTs and the temporally normalized LSTs for the tile h26v04.

RMSE (K)	Daytime	Nighttime
ATCH (with the original LSTs)	3.4	2.8
ATCH (with normalized LSTs)	3.1	2.6

coefficient  $r$  of 0.89. In addition, the incorporation of the NDVI and a single multiplier (i.e., the ATCE) is insufficient to fully capture  $\Delta T_{\text{air}}$  (refer to Fig. A1b1), because  $\Delta T_{\text{air}}$  is determined simultaneously by various meteorological and surface conditions (Fu and Weng, 2018). Consequently, more factors such as the albedo, soil moisture, and relative humidity should be incorporated (i.e., as conducted by the ATCH) (Lin et al., 2016; Kloog et al., 2014; Good, 2016).

## Appendix B. Effect of diurnal observation time on prediction accuracy

This appendix includes one table (Table B1) and one figure (Fig. B1) that demonstrate the uncertainty of ATC modelling due to the observation time difference for daily MODIS LSTs. Taking Terra/MODIS tile h26v04 as an example (the variation of the observation time can exceed 2 h), we normalized all the daytime (nighttime) LSTs to those at 10:30 (22:30) by using the temporal normalization model proposed by Duan et al. (2014). The results listed in Table B1 and Fig. B1 indicate that the LST normalization procedure slightly improves the accuracy of ATC modelling (by around 0.3 K for both daytime and nighttime), but the improvement may occasionally be minimal (e.g., Fig. B1c).

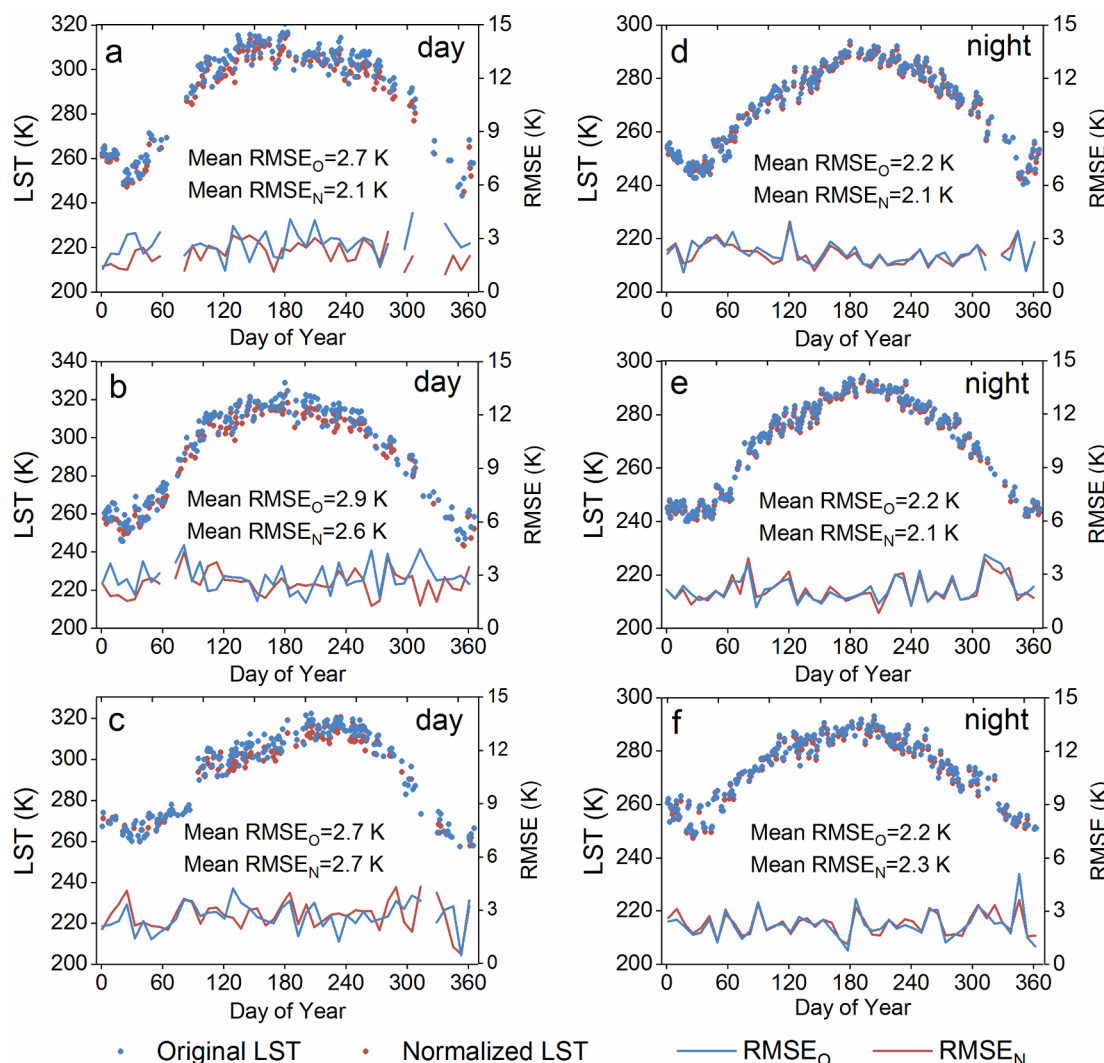


**Fig. B1.** Modelling accuracy of the ATCH determined using the original and temporally normalized LSTs (for MODIS tile h26v04) at three randomly selected pixels in daytime (first column, a–c) and nighttime (second column, d–f). The RMSE<sub>O</sub> and RMSE<sub>N</sub> represent the errors using the original and temporally-normalized LSTs, respectively.

## References

- Aires, F., Prigent, C., Rossow, W.B., 2004. Temporal interpolation of global surface skin temperature diurnal cycle over land under clear and cloudy conditions. *J. Geophys. Res.* 109, D04313. <https://doi.org/10.1029/2003JD003527>.
- Bechtel, B., 2011. Multitemporal Landsat data for urban heat island assessment and classification of local climate zones. In: Proceedings of the IEEE Joint Urban Remote Sensing Event (JURSE), Munich, Germany, pp. 129–132.
- Bechtel, B., 2012. Robustness of annual cycle parameters to characterize the urban thermal landscapes. *IEEE Geosci. Remote Sens. Lett.* 9 (5), 876–880. <https://doi.org/10.1109/lgrs.2012.2185034>.
- Bechtel, B., Sismanidis, P., 2017. Time series analysis of moderate resolution land surface temperatures. In: Weng, Q. (Ed.), *Remote Sensing: Time Series Image Processing*. Taylor and Francis.
- Benali, A., Carvalho, A.C., Nunes, J.P., Carvalhais, N., Santos, A., 2012. Estimating air surface temperature in Portugal using MODIS LST data. *Remote Sens. Environ.* 124

- (9), 108–121. <https://doi.org/10.1016/j.rse.2012.04.024>.
- Brooks, E.B., Thomas, V.A., Wynne, R.H., Coulston, J.W., 2012. Fitting the multitemporal curve: a Fourier series approach to the missing data problem in remote sensing analysis. *IEEE Trans. Geosci. Remote Sens.* 50 (9), 3340–3353. <https://doi.org/10.1109/TGRS.2012.2183137>.
- Crosson, W.L., Al-Hamdan, M.Z., Hemmings, S.N.J., Wade, G.M., 2012. A daily merged MODIS Aqua-Terra land surface temperature data set for the conterminous United States. *Remote Sens. Environ.* 119 (8), 315–324. <https://doi.org/10.1016/j.rse.2011.12.019>.
- Duan, S.B., Li, Z.L., Wang, N., Wu, H., Tang, B.H., 2012. Evaluation of six land-surface diurnal temperature cycle models using clear-sky in situ and satellite data. *Remote Sens. Environ.* 124 (2), 15–25. <https://doi.org/10.1016/j.rse.2012.04.016>.
- Duan, S.B., Li, Z.L., Tang, B.H., Wu, H., Tang, R., 2014. Generation of a time-consistent land surface temperature product from MODIS data. *Remote Sens. Environ.* 140, 339–349. <https://doi.org/10.1016/j.rse.2013.09.003>.
- Duan, S.B., Li, Z.L., Leng, P., 2017. A framework for the retrieval of all-weather land surface temperature at a high spatial resolution from polar-orbiting thermal infrared and passive microwave data. *Remote Sens. Environ.* 195, 107–117. <https://doi.org/10.1016/j.rse.2017.04.008>.
- Fan, X.M., Liu, H.G., Liu, G.H., Li, S.B., 2014. Reconstruction of MODIS land-surface temperature in a flat terrain and fragmented landscape. *Int. J. Remote Sens.* 35 (23), 7857–7877. <https://doi.org/10.1080/01431161.2014.978036>.
- Fan, X., Tang, B.H., Wu, H., Yan, G., Li, Z.L., 2015. Daytime land surface temperature extraction from MODIS thermal infrared data under cirrus clouds. *Sensors* 15 (5), 9942–9961. <https://doi.org/10.3390/s150509942>.
- Fu, P., Weng, Q., 2015. Temporal dynamics of land surface temperature from Landsat TIR time series images. *IEEE Geosci. Remote Sens. Lett.* 12 (10), 2175–2179. <https://doi.org/10.1109/LGRS.2015.2455019>.
- Fu, P., Weng, Q., 2016. Consistent land surface temperature data generation from irregularly spaced Landsat imagery. *Remote Sens. Environ.* 184, 175–187. <https://doi.org/10.1016/j.rse.2016.06.019>.
- Fu, P., Weng, Q., 2018. Variability in annual temperature cycle in the urban areas of the United States as revealed by MODIS imagery. *ISPRS J. Photogramm. Remote Sens.* 146, 65–73. <https://doi.org/10.1016/j.isprsjprs.2018.09.003>.
- Gallo, K., Hale, R., Tarpley, D., Yu, Y., 2011. Evaluation of the relationship between air and land surface temperature under clear- and cloudy-sky conditions. *J. Appl. Meteorol. Climatol.* 50 (3), 767–775. <https://doi.org/10.1175/2010JAMC2460.1>.
- Good, E.J., 2016. An in situ-based analysis of the relationship between land surface “skin” and screen-level air temperatures. *J. Geophys. Res. Atmos.* 121 (15), 8801–8819. <https://doi.org/10.1002/2016JD025318>.
- Good, E.J., Ghent, D.J., Bulgin, C.E., Remedios, J.J., 2017. A spatiotemporal analysis of the relationship between near-surface air temperature and satellite land surface temperatures using 17 years of data from the ATSR series. *J. Geophys. Res.-Atmos.* 122 (17), 9185–9210. <https://doi.org/10.1002/2017JD026880>.
- Hengl, T., Heuvelink, G.B.M., Tadić, M.P., Pebesma, E.J., 2012. Spatio-temporal prediction of daily temperatures using time-series of MODIS LST images. *Theor. Appl. Climatol.* 107 (1–2), 265–277. <https://doi.org/10.1007/s00704-011-0464-2>.
- Huang, F., Zhan, W., Voogt, J., Hu, L., Wang, Z., Quan, J., 2016. Temporal upscaling of surface urban heat island by incorporating an annual temperature cycle model: a tale of two cities. *Remote Sens. Environ.* 186, 1–12. <https://doi.org/10.1016/j.rse.2016.08.009>.
- Jin, M., Dickinson, R.E., Zhang, D.L., 2005. The footprint of urban areas on global climate as characterized by MODIS. *J. Climate* 18, 1551–1565. <https://doi.org/10.1175/JCLI3344.1>.
- Jin, M.S., Mullens, T., 2014. A study of the relations between soil moisture, soil temperatures and surface temperatures using arm observations and offline clm4 simulations. *Climate* 2 (4), 279–295. <https://doi.org/10.3390/cli2040279>.
- Kalma, J.D., McVicar, T.R., McCabe, M.F., 2008. Estimating land surface evaporation: a review of methods using remotely sensed surface temperature data. *Surv. Geophys.* 29 (4–5), 421–469. <https://doi.org/10.1007/s10712-008-9037-z>.
- Ke, L., Ding, X., Song, C., 2013. Reconstruction of time-series MODIS LST in central Qinghai-Tibet Plateau using geostatistical approach. *IEEE Geosci. Remote Sens. Lett.* 10, 1602–1606. <https://doi.org/10.1109/LGRS.2013.2263553>.
- Kleidon, A., Renner, M., 2013. A simple explanation for the sensitivity of the hydrologic cycle to surface temperature and solar radiation and its implications for global climate change. *Earth Syst. Dynam.* 4 (2), 455–465. <https://doi.org/10.5194/esd-4-455-2013>.
- Kloog, I., Nordio, F., Coull, B.A., Schwartz, J., 2014. Predicting spatiotemporal mean air temperature using MODIS satellite surface temperature measurements across the northeastern USA. *Remote Sens. Environ.* 150 (7), 132–139. <https://doi.org/10.1016/j.rse.2014.04.024>.
- Kou, X., Jiang, L., Bo, Y., Yan, S., Chai, L., 2016. Estimation of land surface temperature through blending MODIS and AMSR-E data with the Bayesian maximum entropy method. *Remote Sens.* 8 (2), 105. <https://doi.org/10.3390/rs8020105>.
- Li, S., Yu, Y., Sun, D., Dan, T., Zhan, X., Long, C., 2014. Evaluation of 10 year AQUA/MODIS land surface temperature with SURFRAD observations. *Int. J. Remote Sens.* 35 (3), 830–856. <https://doi.org/10.1080/01431161.2013.873149>.
- Li, X., Zhou, Y., Asrar, G.R., Zhu, Z., 2018a. Creating a seamless 1 km resolution daily land surface temperature dataset for urban and surrounding areas in the conterminous United States. *Remote Sens. Environ.* 206, 84–97. <https://doi.org/10.1016/j.rse.2017.12.010>.
- Li, X., Zhou, Y., Asrar, G.R., Zhu, Z., 2018b. Developing a 1 km resolution daily air temperature dataset for urban and surrounding areas in the conterminous United States. *Remote Sens. Environ.* 215, 74–84. <https://doi.org/10.1016/j.rse.2018.05.034>.
- Li, Z.L., Tang, B.H., Wu, H., Ren, H., Yan, G., Wan, Z., 2013. Satellite-derived land surface temperature: current status and perspectives. *Remote Sens. Environ.* 131 (131), 14–37. <https://doi.org/10.1016/j.rse.2012.12.008>.
- Lin, X., Zhang, W., Huang, Y., Sun, W., Han, P., Yu, L., et al., 2016. Empirical estimation of near-surface air temperature in china from MODIS LST data by considering physiographic features. *Remote Sens.* 8 (8), 629. <https://doi.org/10.3390/rs808629>.
- Lin, Y., 2011. Maximal linear range of linear transformer analysis using maple & lstop. In: IEEE Second International Conference on Mechanic Automation and Control Engineering, pp. 7453–7456. <https://doi.org/10.1109/MACE.2011.5988773>.
- Liu, Z., Wu, P., Duan, S., Zhan, W., Ma, X., Wu, Y., 2017. Spatiotemporal reconstruction of land surface temperature derived from FengYun geostationary satellite data. *IEEE J. Sel. Top. Appl. Earth Obs. Remote Sens.* 10 (10), 4531–4543. <https://doi.org/10.1109/JSTARS.2017.2716376>.
- Lu, L., Venus, V., Skidmore, A., Wang, T., Luo, G., 2011. Estimating land-surface temperature under clouds using MSG/SEVIRI observations. *Int. J. Appl. Earth Obs. Geoinf.* 13 (2), 265–276. <https://doi.org/10.1016/j.jag.2010.12.007>.
- Lyon, S.W., Sørensen, R., Stendahl, J., Seibert, J., 2010. Using landscape characteristics to define an adjusted distance metric for improving kriging interpolations. *Int. J. Geogr. Inf. Sci.* 24 (5), 723–740. <https://doi.org/10.1080/13658810903062487>.
- Mildrexler, D.J., Zhao, M., Running, S.W., 2011. A global comparison between station air temperatures and MODIS land surface temperatures reveals the cooling role of forests. *J. Geophys. Res.* 116, G03025. <https://doi.org/10.1029/2010JG001486>.
- Murray, K., Conner, M., 2009. Methods to quantify variable importance: implications for the analysis of noisy ecological data. *Ecology* 90 (2), 348–355. <https://doi.org/10.1016/j.patrec.2010.03.014>.
- Nojarov, P., 2012. Variations in precipitation amounts, atmosphere circulation, and relative humidity in high mountainous parts of Bulgaria for the period 1947–2008. *Theor. Appl. Climatol.* 107 (1–2), 175–187. <https://doi.org/10.1007/s00704-011-0473-1>.
- Pede, T., Mountrakis, G., 2018. An empirical comparison of interpolation methods for MODIS 8-day land surface temperature composites across the conterminous units states. *ISPRS J. Photogramm. Remote Sens.* 142, 137–150. <https://doi.org/10.1016/j.isprsjprs.2018.06.003>.
- Quan, J., Zhan, W., Chen, Y., Wang, M., Wang, J., 2016. Time series decomposition of remotely sensed land surface temperature and investigation of trends and seasonal variations in surface urban heat islands. *J. Geophys. Res. Atmos.* 121 (6), 2638–2657. <https://doi.org/10.1002/2015JD024354>.
- Quan, J., Zhan, W., Ma, T., Du, Y., Guo, Z., Qin, B., 2018. An integrated model for generating hourly Landsat-like land surface temperatures over heterogeneous landscapes. *Remote Sens. Environ.* 206, 403–423. <https://doi.org/10.1016/j.rse.2017.12.003>.
- Sismanidis, P., Keramitsoglou, I., Bechtel, B., Kiranoudis, C.T., 2017. Improving the downscaling of diurnal land surface temperatures using the annual cycle parameters as disaggregation kernels. *Remote Sens.* 9 (1), 23. <https://doi.org/10.3390/rs9010023>.
- Sandholt, I., Rasmussen, K., Andersen, J., 2002. A simple interpretation of the surface temperature/vegetation index space for assessment of surface moisture status. *Remote Sens. Environ.* 79 (2–3), 213–224. [https://doi.org/10.1016/S0034-4257\(01\)00274-7](https://doi.org/10.1016/S0034-4257(01)00274-7).
- Schmidt, A., Bandar, Z., 1998. A Modular Neural Network Architecture with Additional Generalization Abilities for Large Input Vectors. *Artificial Neural Nets and Genetic Algorithms*, Springer Vienna.
- Shamir, E., Georgakakos, K.P., 2014. MODIS land surface temperature as an index of surface air temperature for operational snowpack estimation. *Remote Sens. Environ.* 152 (152), 83–98. <https://doi.org/10.1016/j.rse.2014.06.001>.
- Sun, L., Chen, Z., Gao, F., Anderson, M., Song, L., Wang, L., 2017. Reconstructing daily clear-sky land surface temperature for cloudy regions from MODIS data. *Comput. Geosci.* 105, 10–20. <https://doi.org/10.1016/j.cageo.2017.04.007>.
- Wan, Z., Zhang, Y., Zhang, Q., Li, Z., 2002. Validation of the land-surface temperature products retrieved from Terra Moderate Resolution Imaging Spectroradiometer data. *Remote Sens. Environ.* 83 (1–2), 163–180. [https://doi.org/10.1016/S0034-4257\(02\)00093-7](https://doi.org/10.1016/S0034-4257(02)00093-7).
- Weng, Q., 2009. Thermal infrared remote sensing for urban climate and environmental studies: methods, applications, and trends. *ISPRS J. Photogramm. Remote Sens.* 64 (4), 335–344. <https://doi.org/10.1016/j.isprsjprs.2009.03.007>.
- Weng, Q., Fu, P., Gao, F., 2014. Generating daily land surface temperature at Landsat resolution by fusing Landsat and MODIS data. *Remote Sens. Environ.* 145 (8), 55–67. <https://doi.org/10.1016/j.rse.2014.02.003>.
- Wongsai, N., Wongsai, S., Huete, A., 2017. Annual seasonality extraction using the cubic spline function and decadal trend in temporal daytime MODIS LST data. *Remote Sens.* 9 (12), 1254. <https://doi.org/10.3390/rs9121254>.
- Xu, Y., Shen, Y., 2013. Reconstruction of the land surface temperature time series using harmonic analysis. *Comput. Geosci.* 61 (4), 126–132. <https://doi.org/10.1016/j.cageo.2013.08.009>.
- Yang, Y., Cai, W., Yang, J., 2017. Evaluation of MODIS land surface temperature data to estimate near-surface air temperature in northeast china. *Remote Sens.* 9 (5), 410. <https://doi.org/10.3390/rs9050410>.

- Yu, W., Ma, M., Wang, X., Tan, J., 2014. Estimating the land-surface temperature of pixels covered by clouds in MODIS products. *J. Appl. Remote Sens.* 8 (14), 083525. <https://doi.org/10.1117/1.JRS.8.083525>.
- Zeng, C., Long, D., Shen, H., Wu, P., Cui, Y., Hong, Y., 2018. A two-step framework for reconstructing remotely sensed land surface temperatures contaminated by cloud. *ISPRS J. Photogramm. Remote Sens.* 141, 30–45. <https://doi.org/10.1016/j.isprsjprs.2018.04.005>.
- Zhan, W., Huang, F., Quan, J., Zhu, X., Gao, L., Zhou, J., 2016. Disaggregation of remotely sensed land surface temperature: a new dynamic methodology. *J. Geophys. Res. Atmos.* 121 (18), 414–421. <https://doi.org/10.1002/2016JD024891>.
- Zhang, H., Zhang, F., Ye, M., Che, T., Zhang, G., 2016. Estimating daily air temperatures over the Tibetan plateau by dynamically integrating MDOIS LST data. *J. Geophys. Res. Atmos.* 121 (19), 11425–11441. <https://doi.org/10.1002/2016JD025154>.
- Zhang, X., Liang, S., Zhou, G., Wu, H., Zhao, X., 2014. Generating global land surface satellite incident shortwave radiation and photosynthetically active radiation products from multiple satellite data. *Remote Sens. Environ.* 152 (152), 318–332. <https://doi.org/10.1016/j.rse.2014.07.003>.
- Zhang, X., Pang, J., Li, L., 2015. Estimation of land surface temperature under cloudy skies using combined diurnal solar radiation and surface temperature evolution. *Remote Sens.* 7 (1), 905–921. <https://doi.org/10.3390/rs70100905>.
- Zheng, J., Yin, Y., Li, B., 2010. A new scheme for climate regionalization in China. *Acta Geogr. Sin.* 65 (1), 3–13.
- Zhou, Y., Qin, Z., Bao, G., 2012. Land surface temperature estimation under cloud cover with GIDS. *J. Remote Sens.* 16 (3), 492–504. <https://doi.org/10.1007/s10001-012-0349-2>.
- Zou, Z., Zhan, W., Liu, Z., Bechtel, B., Gao, L., Hong, F., 2018. Enhanced modeling of annual temperature cycle with temporally discrete remotely sensed thermal observations. *Remote Sens.* 10 (4), 650. <https://doi.org/10.3390/rs10040650>.